



1 **Susceptibility of Marine Warm Clouds to Aerosols in
2 Different Monsoon Periods over the South China Sea**

3 Yan Liu¹, Hailing Jia², Yong Han^{1*}

4 ¹Advanced Science & Technology of Space and Atmospheric Physics Group (ASAG), School of
5 Atmospheric Sciences, Sun Yat-sen University, 519082 Zhuhai, China

6 ²SRON Space Research Organisation Netherlands, Leiden, The Netherlands

7 *Correspondence to: Yong Han (hany66@mail.sysu.edu.cn)

8



9 **Abstract.**

10 Understanding the susceptibility of warm clouds to aerosol loading, quantified by the aerosol–cloud
11 interactions (ACI) index, is essential for assessing ACI and their climate impacts. Previous studies have
12 demonstrated that this susceptibility is strongly modulated by environmental conditions. The South
13 China Sea (SCS), influenced alternately by the southwest and northeast monsoons, provides a unique
14 natural laboratory for examining ACI under contrasting thermodynamic and moisture conditions. We
15 utilized long-term satellite observations and reanalysis datasets to investigate ACI over the SCS, with a
16 focus on non-raining warm liquid clouds. Based on large-scale circulation patterns and moisture
17 conditions, the monsoon system over the SCS is categorized into three phases: the southwest monsoon
18 wet period (SWMW), the northeast monsoon wet period (NEMW), and the northeast monsoon dry period
19 (NEMD). The robust Twomey effect was observed across all three periods. The ACI intensity strengthens
20 progressively from SWMW to NEMW and further to NEMD, corresponding to the transition from moist,
21 convectively active to dry, stably stratified environments. This transition is governed by variations in
22 water-vapor availability and lower-tropospheric stability (LTS), where stable conditions may enhance
23 ACI through aerosol accumulation, while moist environments are likely to weaken it via enhanced
24 condensational and coalescence growth. These findings reveal the dominant roles of thermodynamic
25 stability and moisture in regulating ACI over the SCS. The interplay among aerosols, humidity, and
26 stability governs marine warm-cloud microphysics in tropical monsoon environments, providing
27 observational constraints for improving the representation of ACI in climate models.

28

29 **1 Introduction**

30 Aerosol–cloud interactions (ACI) play a crucial role in regulating Earth's radiative balance and
31 hydrological cycle by altering cloud microphysical and macrophysical properties (Bellouin et al., 2020;
32 Jia et al., 2021; Rosenfeld et al., 2019; Stier et al., 2024; Wang et al., 2024c; Zhao et al., 2024). Numerous
33 studies have demonstrated that ACI are strongly modulated by environmental conditions, such as lower-
34 tropospheric stability (Chen et al., 2014; Wang et al., 2014), relative humidity (Douglas and L'Ecuyer,
35 2019), precipitable water vapor (Qiu et al., 2017; Yuan et al., 2008; Zheng et al., 2022), vertical velocity



36 (Jia et al., 2022; Su et al., 2010), wind shear (Fan et al., 2009; Kim et al., 2003), and the vertical overlap
37 between aerosol and cloud layers (Costantino and Bréon, 2013). However, over the South China Sea
38 (SCS), a region strongly influenced by pronounced monsoon circulation, the observational evidence of
39 how ACI respond to variations in thermodynamic and moisture conditions remains limited.

40 The SCS, one of the world's largest marginal seas, provides a unique natural laboratory for investigating
41 ACI under the alternating influence of two opposing monsoon systems. The SCS experiences a
42 pronounced seasonal reversal of wind regimes, characterized by a warm, moist southwest monsoon
43 during boreal summer and a cool, dry northeast monsoon during boreal winter (Wang et al., 2009).

44 During the southwest monsoon period, the marine boundary layer over the northern SCS becomes
45 unstable, with enhanced air-sea temperature differences and surface turbulent heat fluxes that intensify
46 vertical mixing and deepen the boundary layer while reducing wind shear (Peng et al., 2016). Rainfall
47 during this period is primarily governed by warm-cloud microphysical processes and vapor convergence-
48 driven condensation (Wang et al., 2007). In contrast, during the northeast monsoon period, cold surges
49 associated with the East Asian winter monsoon substantially modify the SCS boundary-layer structure
50 by enhancing surface turbulent fluxes, deepening the mixed layer, and strengthening the inversion that
51 promotes extensive low-cloud development (Wang et al., 2024a). The SCS is also a region that is
52 simultaneously affected by various types of aerosols from industrial emissions, shipping activities, and
53 biomass burning. It has been shown that those aerosols substantially modify the microphysical structure
54 of marine boundary layer clouds over the SCS by increasing small droplet concentrations and suppressing
55 midsize droplets near cloud base (Miller et al., 2023). Recent shipborne observations further reveal that
56 aerosol sources over the SCS exhibit distinct seasonal contrasts, being dominated by continental outflow
57 from mainland Southeast Asia during the southwest monsoon and by pollution plumes transported from
58 continental China during the northeast monsoon (Ou et al., 2025). Yet, how these contrasting aerosol and
59 meteorological regimes modulate ACI, particularly for warm non-raining clouds, remains poorly
60 quantified.

61 Quantifying ACI is essential for constraining their climatic impacts. According to the Sixth Assessment
62 Report of the Intergovernmental Panel on Climate Change (Douville et al., 2023), the effective radiative
63 forcing associated with ACI (ERF_{aci}) is estimated to be -0.84 W m^{-2} globally, with a wide 5–95%



64 confidence range from -1.45 W m^{-2} to -0.25 W m^{-2} , dominating the overall uncertainty in total aerosol
65 effective radiative forcing, which ranges between -1.7 and -0.4 W m^{-2} . ERF_{aci} may be further
66 decomposed into two components: the instantaneous radiative forcing due to ACI, also known as the
67 Twomey effect (RF_{aci} , Twomey, 1977, 1974), and rapid adjustments (Ackerman et al., 2004; Albrecht,
68 1989; Bellouin et al., 2020). To quantify the cloud response to aerosol perturbations, Feingold et al. (2001)
69 proposed the ACI index (ACI_r and ACI_{Nd}), which has since become a widely used metric for evaluating
70 the strength of the Twomey effect in both satellite and in-situ studies, defined as:

71
$$\text{ACI}_r = -d \ln r / d \ln N_{\text{CCN}} \quad (1)$$

72
$$\text{ACI}_{\text{Nd}} = d \ln N_d / 3d \ln N_{\text{CCN}} \quad (2)$$

73 where r and N_d denote the cloud effective radius and droplet number concentration, respectively, and
74 N_{CCN} represents a proxy for cloud condensation nuclei (CCN) number concentration. ACI_{Nd} is more
75 recently also referred to as the Nd susceptibility to aerosols (Ma et al., 2018a, b).

76 Although many studies have examined the environmental modulation of ACI over both oceanic and
77 continental regions (Fan et al., 2016; Jia et al., 2019, 2022; Jia and Quaas, 2023; Seinfeld et al., 2016;
78 Sorooshian et al., 2019; Wall et al., 2022; Wang et al., 2024d), such processes remain poorly constrained
79 over the SCS. The pronounced seasonal reversal of monsoon circulation in this region creates highly
80 contrasting thermodynamic and moisture conditions, along with differing aerosol regimes, which
81 together exert distinct influences on cloud microphysics and modulate the ACI processes. Therefore, this
82 study aims to provide a comprehensive assessment of ACI in non-raining warm clouds over the SCS
83 under different monsoon regimes. Long-term multi-satellite and reanalysis datasets from July 2002 to
84 February 2023 are integrated to characterize variations in aerosol, cloud, and environmental properties
85 across the southwest monsoon wet (SWMW), northeast monsoon wet (NEMW), and northeast monsoon
86 dry (NEMD) phases, and to quantitatively evaluate the corresponding ACI responses. Particular attention
87 is given to understanding how variations in water vapor availability and lower-tropospheric stability
88 (LTS) influence the sensitivity of cloud microphysical responses to aerosol perturbations.

89 The paper is organized as follows. Section 2 describes the datasets and method used in this study. The
90 main findings and related discussions are presented in Section 3. Section 4 summarizes the key findings
91 and conclusions.



92 **2 Data and Methods**

93 This study employs long-term, multi-source datasets to investigate ACI over the SCS. The cloud
94 properties are derived from the Clouds and the Earth's Radiant Energy System (CERES)–Moderate
95 Resolution Imaging Spectroradiometer(MODIS) Edition 4 Level-3 product(SSF1deg, Aqua, daytime).
96 Aerosol information is obtained from the Modern-Era Retrospective analysis for Research and
97 Applications, Version 2 (MERRA-2). Meteorological fields are taken from the European Centre for
98 Medium-Range WeatherForecasts (ECMWF) fifth-generation reanalysis (ERA5). Precipitation data are
99 provided by the Integrated Multi-satellite Retrievals for GPM (IMERG) Version 7 Final Run, and sea
100 surface temperature (SST) data are obtained from the National Oceanic and Atmospheric Administration
101 (NOAA) Optimum Interpolation (OI) SST, version 2.
102

Table 1: Overview of datasets used in this study.

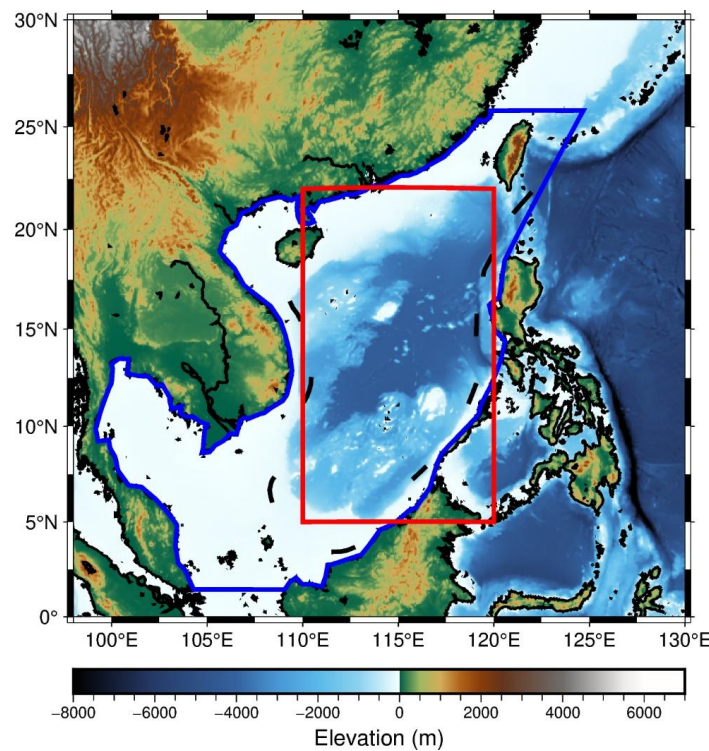
Parameter	Data Source	Spatial Resolution	Temporal Resolution	Data Range
Cloud Effective Radius	CERES–MODIS	$1^\circ \times 1^\circ$	daily	Jul 2002 – Feb 2023
Cloud Optical Thickness	V04 SSF1deg			
Cloud-top Temperature	(Aqua, daytime)			
Cloud-top Pressure				
Liquid Cloud Area Fraction				
Liquid Water Path				
Total aerosol extinction AOT (550 nm)	MERRA-2	0.5° 0.625°	× daily	Jul 2002 – Feb 2023
Total aerosol Ångström parameter (470–870 nm)				
Specific Humidity	ERA5	0.25°	× daily	Jul 2002 – Feb 2023
Temperature		0.25°		
horizontal wind components				
mean sea level pressure				
Precipitation	IMERG V07 Final	$0.1^\circ \times 0.1^\circ$	30 min	Jul 2002 – Feb 2023
Sea Surface Temperature	NOAA OI SST V2	$1^\circ \times 1^\circ$	monthly	Jul 2002 – Feb 2023

103 **2.1 Study Area**

104 SCS is one of the world's largest marginal seas, characterized by complex air–sea interactions and a
105 pronounced seasonal reversal of wind systems (Wang et al., 2009). This region is strongly influenced by



106 the Asian monsoon circulation, exhibiting distinct southwest and northeast monsoon regimes that
107 profoundly modulate its thermodynamic and dynamic environments (Zheng et al., 2025). These
108 alternating monsoon circulations govern the regional aerosol loading (Ou et al., 2025), boundary-layer
109 structure (Chen et al., 2025; Peng et al., 2016; Wang et al., 2024a), and cloud microphysical processes
110 (Miller et al., 2023; Wang et al., 2024b), making the SCS an ideal natural laboratory for investigating
111 ACI under contrasting meteorological conditions. In this study, the analysis domain (blue polygon in Fig.
112 1) encompasses the entire SCS, including both coastal and open-ocean areas, to capture the spatial
113 variability of aerosol, cloud, and environmental parameters. The red box in Fig. 1 delineates the
114 subregion (3° – 22° N, 110° – 120° E) used for defining the monsoon regimes following Wang et al. (2004).



115
116 **Figure 1: Study region and monsoon classification over the South China Sea. The blue polygon indicates the**
117 **study domain, while the red box marks the region used for defining the monsoon regimes.**

118 **2.2 Cloud Remote Sensing Products**

119 Cloud retrievals used in this study are derived from the Moderate Resolution Imaging Spectroradiometer
120 (MODIS) aboard the Aqua satellite, which has an equatorial crossing time of approximately 1:30 p.m.



121 local time. The MODIS cloud products analysed are obtained from the Clouds and the Earth's Radiant
122 Energy System (CERES) MODIS (CERES-MODIS hereafter) Edition 4 (Minnis et al., 2011a, 2021)
123 Single Scanner Footprint (SSF) daily products (Level 3, $1^\circ \times 1^\circ$ grid resolution), which provide
124 physically consistent cloud and radiative properties based on synergistic MODIS and CERES
125 observations. The CERES-MODIS cloud retrievals have been extensively validated (Minnis et al.,
126 2011b; Yost et al., 2021) and have been widely employed in studies of ACI (Jia et al., 2021; Painemal
127 2018). CERES-MODIS Edition 4 SSF cloud parameters utilized here include cloud optical depth (τ),
128 cloud effective radius (CER), cloud-top temperature (CTT), cloud-top pressure (CTP), liquid cloud area
129 fraction (LCAF), and liquid water path (LWP). CER is retrieved from the $3.7\text{-}\mu\text{m}$ channel, which is less
130 affected by retrieval biases than its 2.1- and $1.6\text{-}\mu\text{m}$ counterparts (Grosvenor et al., 2018). Following
131 previous studies that derived N_d from the CERES-MODIS L3 product (Dadashazar et al., 2021; Painemal
132 et al., 2021) using an adiabatic formulation (Grosvenor et al., 2018), N_d was calculated as:

$$133 N_d = \frac{\sqrt{5}}{2\pi k} \left(\frac{f_{ad} C_w \tau}{Q_{ext} \rho_w r_e^5} \right)^{1/2} \quad (3)$$

134 Where, k is a constant factor that relates volume radius to CER and is assumed to be 0.8 over the ocean
135 (Martin et al., 1994), ρ_d is the liquid water density, τ is cloud optical depth, r_e is cloud effective radius,
136 Q_{ext} is the dimensionless extinction efficiency factor (assumed to be 2 for liquid droplets), f_{ad} is the
137 adiabatic fraction, set to 0.7, and C_w is the adiabatic lapse rate of liquid water content calculated from
138 the CTT and CTP (Braun et al., 2018) obtained from CERES-MODIS:

$$139 C_w = \left[\frac{(\varepsilon + w_s) w_s l_v}{R_d T^2} \Gamma_m - \frac{g w_s P}{(P - e_s) R_d T} \right] \rho_d \quad (4)$$

140 where, R_d is the ideal gas constant for dry air, ε is the ratio of the gas constants for dry air and water
141 vapor, w_s is the saturation mixing ratio, l_v is the latent heat of vaporization, T is the CTT, Γ_m is the
142 moist adiabatic lapse rate (as defined in the American Meteorological Society's Glossary), g is the
143 gravitational acceleration, P is the CTP, e_s is the saturation vapor pressure of water, and ρ_d is the
144 density of dry air. CTT was used to calculate e_s and l_v , while both CTT and CTP were used to calculate
145 w_s , Γ_m , and ρ_d .



146 **2.3 Aerosol Optical Properties**

147 Aerosol properties used in this study are obtained from the Modern-Era Retrospective Analysis for
148 Research and Applications, Version 2 (MERRA-2, Gelaro et al., 2017), which assimilates a wide range
149 of satellite observations to provide a physically consistent representation of global aerosol distributions.
150 The MERRA-2 aerosol dataset used here includes the total aerosol extinction (AOD, 550 nm) and the
151 total aerosol Ångström parameter (AE, 470-870 nm), with a spatial resolution of $0.5^\circ \times 0.625^\circ$ and a
152 temporal resolution of 1 hour. To ensure spatiotemporal consistency with the CERES-MODIS cloud
153 products, the MERRA-2 aerosol fields at 14:00 local solar time (LST), closest to the Aqua overpass
154 (~13:30 LST), were regridded to a $1^\circ \times 1^\circ$ grid. AOD represents the column-integrated aerosol extinction,
155 whereas AE characterizes the wavelength dependence of AOD and is commonly used as an indicator of
156 aerosol particle size. A higher AE generally indicates dominance of fine-mode aerosols, while a lower
157 AE suggests coarse-mode particles. The aerosol index (AI) is defined as the product of AOD and AE:

$$158 \quad \text{AI} = \text{AOD} \times \text{AE} \quad (5)$$

159 AI, in comparison to AOD, is considered a better parameter for representing aerosols in ACI studies,
160 because it incorporates information on aerosol particle size, which is critical for cloud droplet activation
161 and microphysical properties (Ma et al., 2018b; Nakajima et al., 2001). Therefore, AI is employed in this
162 study as the aerosol proxy in the calculation of ACI.

163 **2.4 Atmospheric Parameters of Weather Fields**

164 Atmospheric fields were obtained from the fifth-generation ECMWF reanalysis (ERA5, Hersbach et al.,
165 2020). ERA5 assimilates a comprehensive suite of ground-based and satellite observations through a
166 state-of-the-art four-dimensional variational data assimilation system, offering physically consistent and
167 dynamically balanced representations of the atmosphere. The dataset used here includes three-
168 dimensional fields of specific humidity and horizontal wind components (U and V) at all standard
169 pressure levels, temperature at 1000 and 700 hPa, and mean sea level pressure. The daily mean specific
170 humidity and wind speed at 850 hPa were used to distinguish the three periods over the SCS (Wang et
171 al., 2004). Wind and humidity fields at all pressure levels were analysed to characterize the large-scale
172 atmospheric circulation and vertical moisture structure during these periods. The 1000 hPa specific



173 humidity was employed as a proxy for the ambient water vapor available to warm clouds (Dadashazar et
174 al., 2020). Temperatures at 1000 and 700 hPa were used to compute the LTS, which quantifies the
175 thermodynamic stability of the lower atmosphere (Klein and Hartmann, 1993), as follows:

176

$$LTS = \theta_{700\text{hPa}} - \theta_{1000\text{hPa}} \quad (6)$$
$$\theta = T \left(\frac{P_{00}}{P} \right)^{\frac{R}{C_p}}$$

178 where θ_{700} and θ_{1000} denote the potential temperatures at 700 and 1000 hPa, respectively, P_{00} is the
179 standard reference pressure (typically 1000 hPa), P is the pressure at a given level, R is the gas constant
180 for dry air, and C_p is the specific heat capacity of dry air at constant pressure. To ensure spatiotemporal
181 consistency with the aerosol and cloud parameters, both the 1000 hPa specific humidity and LTS at 14:00
182 LST were regredded to a $1^\circ \times 1^\circ$ grid. Sea surface temperature (SST) was obtained from the National
183 Oceanic and Atmospheric Administration (NOAA) Optimum Interpolation SST, version 2 (OI SST v2,
184 Reynolds et al., 2002), which incorporates both in-situ and satellite observations and provides monthly
185 fields at $1^\circ \times 1^\circ$ resolution.

186 **2.5 Precipitation Data**

187 Precipitation data were obtained from the Integrated Multi-satellite Retrievals for GPM (IMERG)
188 Version 07 Final run. IMERG is the flagship precipitation product of the Global Precipitation
189 Measurement (GPM) mission, a collaborative effort between NASA and JAXA (Huffman et al., 2023).
190 The IMERG algorithm calibrates, merges, and interpolates precipitation estimates from the constellation
191 of Low Earth Orbit (LEO) passive microwave (PMW) radiometers onboard GPM satellites. These
192 estimates are subsequently integrated with geostationary satellite infrared observations, particularly in
193 regions with sparse PMW coverage, to produce a global precipitation product with 0.1° spatial and 30-
194 minute temporal resolutions (Huffman et al., 2020; Watters et al., 2021). IMERG precipitation data,
195 owing to its global coverage and high spatiotemporal resolution, have been widely adopted by the
196 research community (Dezfouli et al., 2017; Durden, 2024; Hayden et al., 2023; Tan et al., 2019a; Watters
197 et al., 2021; Watters and Battaglia, 2019; Zhang and Wang, 2024; Zhu et al., 2024). Consequently,

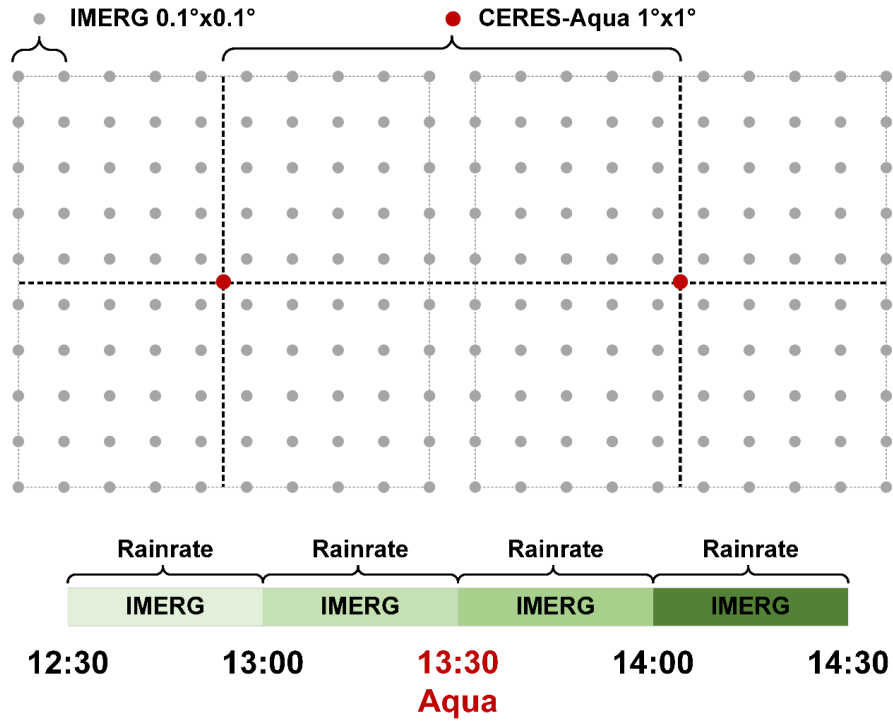


198 IMERG V07 Final Run PrecipitationCal, the gauge-calibrated multi-satellite product, is used here to
199 determine whether precipitation occurred within each CERES–MODIS grid cell.

200 **2.6 Data Quality Control**

201 To minimize the influence of satellite retrieval biases when investigating ACI, a rigorous quality-control
202 procedure was applied to the CERES–MODIS cloud dataset following the method of Saponaro et al.
203 (2017). The selection criteria were as follows:

- 204 1. Only liquid-phase warm clouds were retained, identified by a cloud-phase flag of “liquid” and $CTT >$
205 273 K.
- 206 2. To reduce the impact of large-scale cloud-macrophysical variability and highlight microphysical
207 processes, only clouds with CTP between 650 and 950 hPa were selected.
- 208 3. Thin clouds with $\tau < 5$ were excluded to minimize retrieval uncertainty.
- 209 4. A threshold of $<0.2 \text{ mm h}^{-1}$ was adopted to identify IMERG non-raining cases, following Tan et al.
210 (2019b). The IMERG precipitation data were first collocated onto CERES–MODIS $1^\circ \times 1^\circ$ grid
211 cells. A grid cell was then classified as non-raining when all IMERG sub-pixels within the 13:00–
212 13:30 and 13:30–14:00 local time intervals recorded precipitation rates below 0.2 mm h^{-1} , as
213 illustrated in Fig. 2.



214
215 **Figure 2: Schematic illustration of the procedure used to identify non-raining CERES–MODIS grid cells**
216 **based on IMERG V07 Final Run PrecipitationCal.**

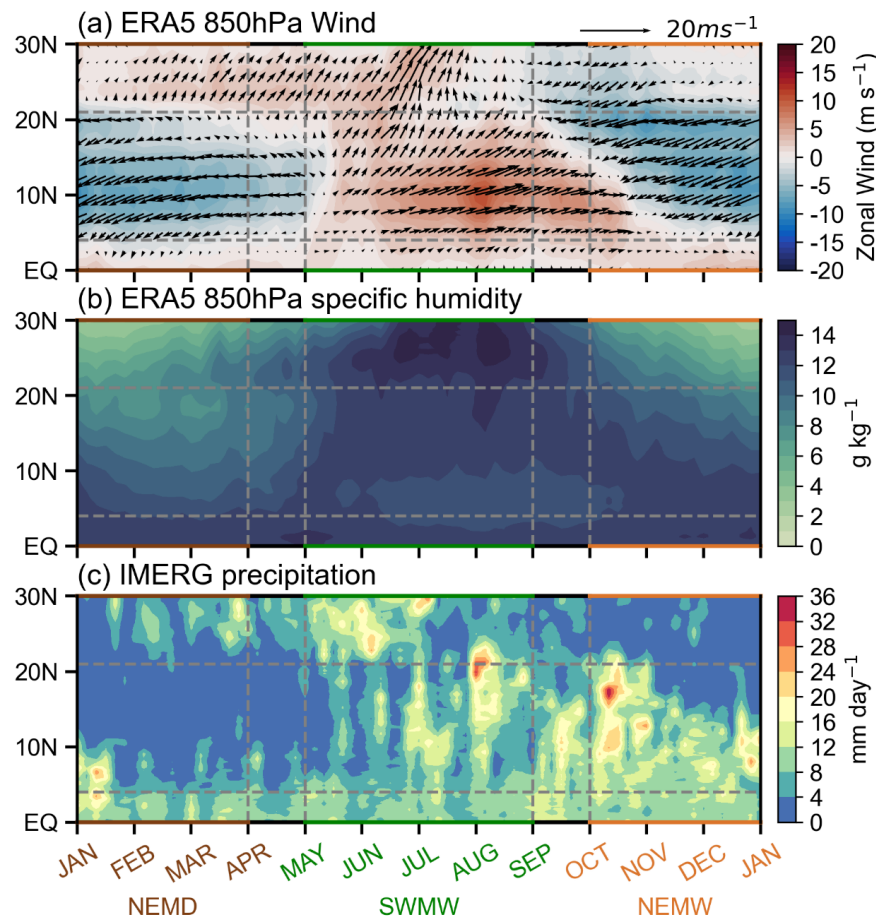
217 **3 Result**

218 **3.1 Definition of Monsoon Periods over the South China Sea**

219 ACI are strongly modulated by environmental factors such as humidity, vertical wind velocity, and
220 atmospheric stability (Zhu et al., 2022). Therefore, considering the prevailing atmospheric conditions is
221 crucial when examining their variability. The atmospheric environment over the SCS exhibits distinct
222 characteristics under the influence of the southwest monsoon and the northeast monsoon. A distinctive
223 feature of the SCS summer monsoon is its nearly simultaneous onset across a broad latitudinal range
224 (3°–22°N) (Wang et al., 2004). On top of the previous studies that defined monsoon periods over the
225 SCS based on wind direction (Wang et al., 2004, 2009), we further incorporated precipitation and specific
226 humidity within this 3–22°N band (the red box in Fig. 1) to classify the study periods into three regimes:
227 the southwest monsoon wet period (SWMW), the northeast monsoon dry period (NEMD), and the
228 northeast monsoon wet period (NEMW). As shown in Fig. 3, the SCS is dominated by the southwest



229 monsoon from May to August, during which specific humidity reaches its maximum and precipitation is
230 strongest. From October to December, the northeast monsoon prevails, accompanied by relatively high
231 specific humidity and intense precipitation. During January to March, the SCS remains under the
232 influence of the northeast monsoon, but specific humidity is at its lowest and precipitation is minimal,
233 representing a dry period. Accordingly, we defined May–August as SWMW, October–December as
234 NEMW, and January–March as NEMD. These three periods not only reflect significant differences in
235 atmospheric circulation and moisture conditions, along with aerosol regimes over the SCS, but also
236 provide distinct environmental backgrounds for ACI, which may influence their characteristics and
237 intensity.



238
239 **Figure 3:** Time-latitude distribution of the (a) ERA5 climatological pentad mean 850 hPa zonal wind (Jul
240 2002–Feb 2023) and (b) ERA5 pentad mean 850 hPa specific humidity (Jul 2002–Feb 2023) and (c) IMERG

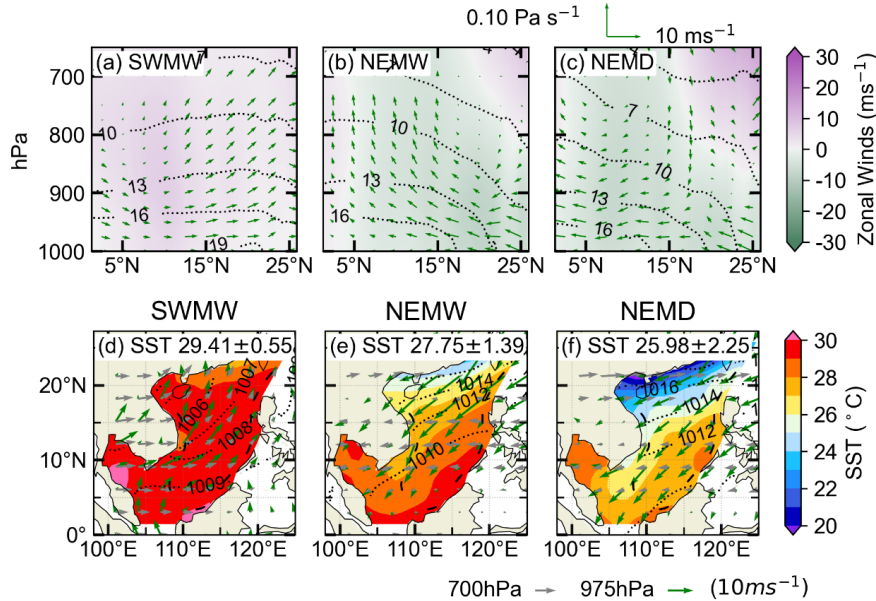


241 pentad mean precipitation (Jul 2002–Feb 2023). The data are averaged over the longitude bands between
242 110E and 120E across the SCS. The arrows in (a) indicates 850hPa horizontal winds.

243 **3.2 Atmospheric conditions and Aerosol–Cloud properties during the Three Periods**

244 **3.2.1 Atmospheric Circulation and Sea Surface Temperature**

245 The Hadley circulation over the SCS is modulated by the Asian monsoon system and the seasonal
246 variation of solar radiation. Fig. 4a shows that during the SWMW period, the SCS is dominated by
247 ascending motion, which is associated with the presence of the IntertropicalConvergence Zone (ITCZ)
248 over the region. During the NEMW period, the Hadley circulation shifts southward and the subtropical
249 high is established over the northern SCS (Fig. 4e). As a result, subsidence dominates the northern part
250 of the region, whereas ascending motion occurs over the equatorial southern part (Fig. 4b). During the
251 NEMD period, as the Hadley circulation continues to shift southward, the subtropical high dominates
252 the SCS (Fig. 4f), leading to prevailing subsidence over the region (Fig. 4c). As shown in Figs. 4a-c, the
253 water vapor content over the SCS gradually decreases from the SWMW period to the NEMW period and
254 further to the NEMD period. During the SWMW period, the winds over the SCS are predominantly
255 westerly. In contrast, during both the NEMW and NEMD periods, the winds are mainly easterly.
256 Additionally, a westerly jet is present at upper levels over the northern SCS. These features show that
257 the SCS exhibits distinct vertical circulation, moisture, and wind patterns under different monsoon
258 conditions.



259

260 **Fig. 4. Zonally averaged cross section of the atmospheric circulation from ERA5 (Jul 2002–Feb 2023) for the**
261 **domain bounded between 110°E and 120°E during (a) the southwest monsoon wet period, (b) the northeast**
262 **monsoon wet period, and (c) the northeast monsoon dry period. Meridional and pressure velocity are denoted**
263 **by arrows (↑ indicates upward motion), whereas colors indicate the zonal wind component. Black contour is**
264 **specific humidity. Panels (d–f) show the corresponding overview of meteorological conditions and SST over**
265 **the SCS region. Color shades represent SST from OISST (Jul 2002–Feb 2023), black contour is sea level**
266 **pressure from ERA5 (Jul 2002–Feb 2023), and arrows are near-surface wind speed at 975 hPa (green) and**
267 **that at 700 hPa (gray) from ERA5 (Jul 2002–Feb 2023).**

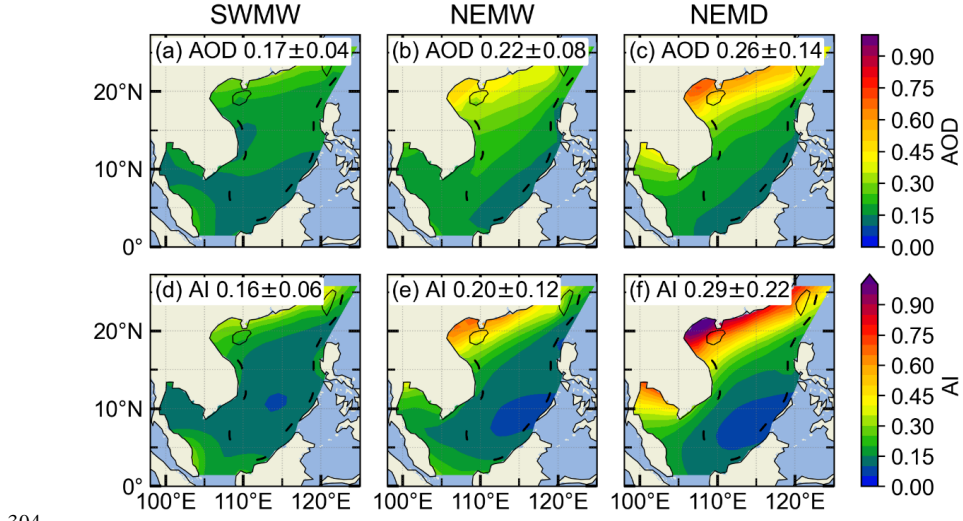
268 The SCS exhibits contrasting large-scale circulation patterns between the southwest and northeast
269 monsoon periods, as shown in Figs. 4d–f. During the SWMW period, the SCS is influenced by tropical
270 and equatorial maritime air masses, with prevailing southwesterlies over the region (Martin and Howland,
271 1982), whereas during the northeast monsoon, winter airflows originating from Siberia and the
272 Mongolian Plateau result in prevailing northeasterlies (Liu et al., 2024). These opposite prevailing wind
273 directions play a crucial role in modulating the transport pathways of continental pollutants into the SCS.
274 Specifically, air masses originating from the Indochinese Peninsula and surrounding Southeast Asian
275 land regions are the primary sources of pollutants transported into the SCS (Miller et al., 2023; Ou et al.,
276 2025; Sun et al., 2023; Zhang et al., 2019), whereas during the northeast monsoon, continental emissions
277 from China may be carried southward into the region (Xiao et al., 2017; Yuan et al., 2024; Zheng et al.,
278 2023).



279 Figures 4d–f show that the area-averaged SST over the SCS is highest during the SWMW period (29.41 ± 0.55 °C), lower during the NEMW period (27.75 ± 1.39 °C), and lowest during the NEMD period (25.98 ± 2.25 °C), with variations consistent with those of specific humidity. During the southwest monsoon, the SST gradient across the SCS is relatively small, whereas during the northeast monsoon, SST decreases with increasing latitude (Wu et al., 2020), and a cold water band forms along the coastal region near mainland China (Chen and Hu, 2023). Higher SST promotes strong latent and sensible heat fluxes, which in turn enhance the atmospheric moisture content over the region (Lee and Park, 2022; Zhang et al., 1995). Consequently, SST and atmospheric moisture exhibit consistent variations across the three periods. In addition, during the northeast monsoon, both the SST (Figs. 4e–f) and atmospheric moisture (Figs. 4b–c) decrease with increasing latitude, showing similar latitudinal gradients.

289 **3.2.2 Aerosol and cloud properties**

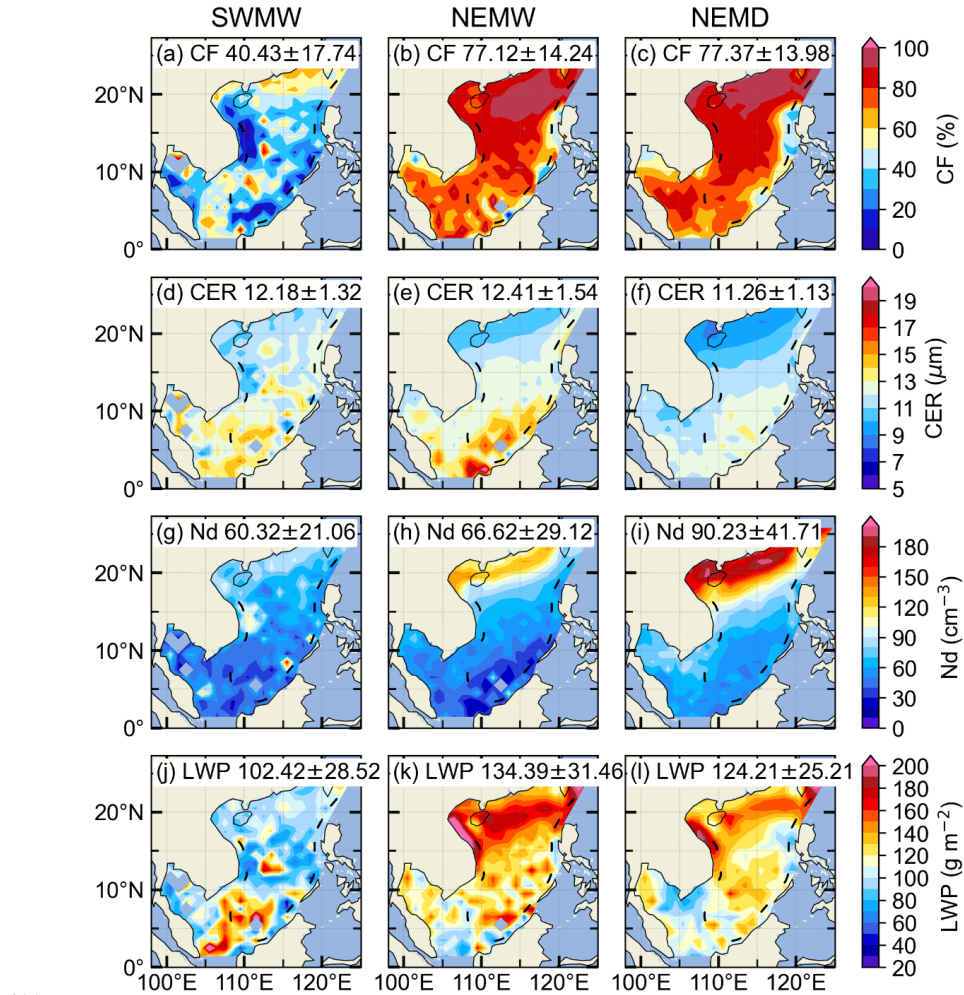
290 The area-averaged aerosol values over the SCS exhibit clear differences among the three periods (Fig. 291 5). The lowest values occur during the SWMW period, with $AOD = 0.17 \pm 0.04$ and $AI = 0.16 \pm 0.06$. 292 Higher values are observed during the NEMW period, with $AOD = 0.22 \pm 0.08$ and $AI = 0.20 \pm 0.12$, 293 whereas the NEMD period shows the highest values, with $AOD = 0.26 \pm 0.14$ and $AI = 0.29 \pm 0.22$, 294 indicating different aerosol sources. Significant differences in aerosol distribution are also observed 295 between the southwest and northeast periods. During the southwest period, higher aerosol values are 296 found in the northern SCS near mainland China and in the southwestern SCS near Malaysia. During the 297 northeast period, aerosol values exhibit a pronounced gradient, forming a coastal band that decreases 298 with increasing distance from the shoreline (Tu et al., 2021). Compared with AOD, AI incorporates 299 aerosol size information and is therefore considered a more suitable proxy for cloud condensation nuclei 300 in studies of ACI (Nakajima et al., 2001). Over the northern SCS near mainland China, AI values are 301 larger than AOD, indicating that aerosols in this region are dominated by fine particles. In contrast, in 302 the central SCS, farther from the continent, AI values are smaller than AOD, suggesting that aerosols 303 there are primarily coarse particles from natural sources.



304

305 **Figure 5: Spatial distributions of MERRA-2 AOD (Jul 2002–Feb 2023) over the South China Sea, averaged**
306 **over different periods: (a) the southwest monsoon wet period, (b) the northeast monsoon wet period, and (c)**
307 **the northeast monsoon dry period. (d–f) Corresponding AI (Jul 2002–Feb 2023) averaged over the same**
308 **periods.**

309 Figure 6 shows the variations in macrophysical and microphysical properties of warm clouds over the
310 SCS during the three monsoon periods. During the SWMW period, the area-averaged warm-cloud
311 fraction over the SCS is the lowest ($40.43 \pm 17.74 \%$), whereas comparable higher values are observed
312 during the NEMW ($77.12 \pm 14.24 \%$) and NEMD ($77.37 \pm 13.98 \%$) periods. Although the SCS
313 experiences the highest water vapor content during the SWMW period, the presence of strong updrafts
314 enhances cloud development (Fig. 4a), leading to the lowest fraction of warm clouds and an increased
315 occurrence of mixed-phase and ice clouds. During the northeast monsoon, the advection of dry and cold
316 continental air over the SCS likely suppresses convective activity, maintaining a higher fraction of warm
317 clouds in the region. Additionally, During the northeast monsoon, the fraction of warm clouds is highest
318 in the northern SCS, whereas lower values are observed in the southern region near the equator, likely
319 due to stronger convective activity in the equatorial area.



320
321 **Figure 6:** Spatial distributions of warm-cloud (a–c) cloud fraction, (d–f) cloud droplet effective radius, (g–i)
322 cloud droplet number concentration, and (j–l) liquid water path over the South China Sea during the
323 southwest monsoon (first column), the northeast monsoon wet period (second column), and the northeast
324 monsoon dry period (third column).

325 The area-averaged warm-cloud droplet effective radius over the SCS is similar across the three monsoon
326 periods, with values of $12.18 \pm 1.32 \mu\text{m}$ during the SWMW period, $12.41 \pm 1.54 \mu\text{m}$ during the NEMW
327 period, and $11.26 \pm 1.13 \mu\text{m}$ during the NEMD period (Figs. 6d–f). In terms of the spatial distribution of
328 warm-cloud droplet effective radius, droplets near the equatorial region tend to be larger than those in
329 other areas, likely due to more pronounced droplet collision and coalescence driven by precipitation,
330 which increases droplet size.



331 The area-averaged warm-cloud droplet number concentration over the SCS exhibits distinct differences
332 among the three periods. The lowest mean value occurs during the SWMW period ($60.32 \pm 21.06 \text{ cm}^{-3}$),
333 followed by a higher value during the NEMW period ($66.62 \pm 29.12 \text{ cm}^{-3}$), and the highest value during
334 the NEMD period ($90.23 \pm 41.71 \text{ cm}^{-3}$) (Figs. 6g–i). The highest cloud droplet number concentration is
335 observed in the northern SCS adjacent to the Chinese mainland, showing a strong spatial correspondence
336 with aerosol distribution. Aerosol concentrations are also largest in this region (Fig. 5), consistent with
337 the Twomey effect, whereby enhanced aerosol loading increases cloud droplet number concentration. In
338 the southern SCS near the equator, cloud droplet number concentration is relatively low, which may be
339 attributed to lower aerosol concentrations and/or stronger convective activity that promotes droplet
340 growth and reduces droplet number.

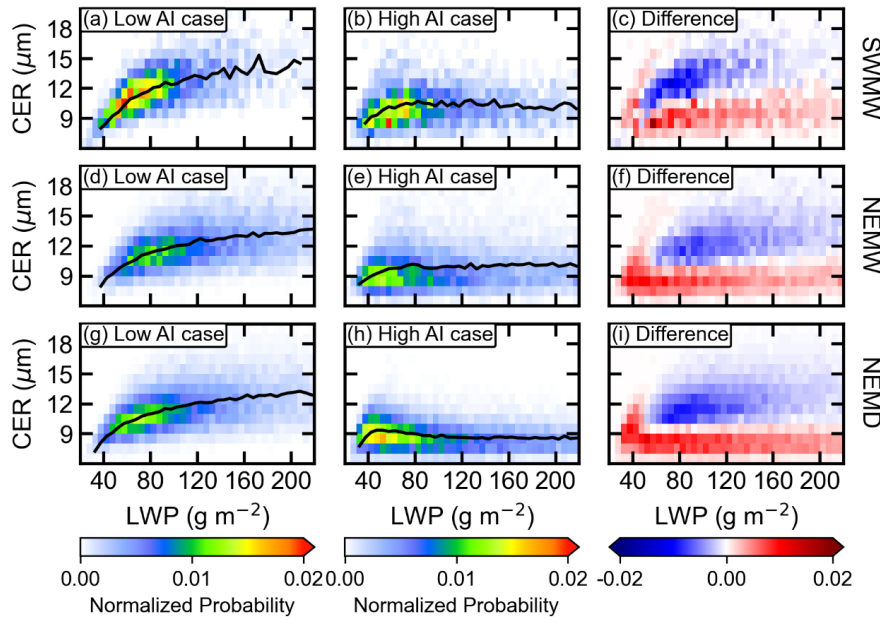
341 The area-averaged warm-cloud LWP over the SCS is lowest during the SWMW period (102.42 ± 28.52
342 g m^{-2}), highest during the NEMW period ($134.39 \pm 31.46 \text{ g m}^{-2}$), and intermediate during the NEMD
343 period ($124.21 \pm 25.21 \text{ g m}^{-2}$) (Figs. 6j–l). During the northeast monsoon, the highest LWP values are
344 observed in the northern SCS adjacent to the Chinese mainland. This may be attributed to more polluted
345 environments, where the second indirect aerosol effect suppresses precipitation, thereby leading to an
346 increase in LWP (Albrecht, 1989). It is noteworthy that the LWP in the northern SCS is higher during
347 the NEMW period than during the NEMD period, which may be associated with sedimentation-
348 entrainment feedback (Ackerman et al., 2004) and/or evaporation-entrainment feedbacks (Dagan et al.,
349 2017; Wang et al., 2003). Compared with the NEMW period, the NEMD period is characterized by
350 higher cloud droplet number concentrations and smaller CER in this region (Fig. 6e, f, h, i). These two
351 feedbacks describe how increased droplet number concentrations and reduced droplet sizes can enhance
352 cloud-top entrainment and evaporation, ultimately leading to a reduction in LWP (Gryspeerdt et al.,
353 2019). Additionally, under drier conditions above cloud tops during the NEMD period, the
354 sedimentation-entrainment feedback may be further amplified, resulting in a stronger reduction in LWP
355 (Gryspeerdt et al., 2019; Sato et al., 2018). During the SWMW, LWP is also relatively high in the
356 southern SCS near the equator (Fig. 6j). In this region, CER is larger and N_d is lower (Figs. 6d, g), likely
357 due to stronger updrafts near the equator, which enhance the vertical development of warm clouds and
358 result in higher cloud water content.



359 Qualitatively, the consistency in zonal gradients of aerosol and cloud properties across all three monsoon
360 regimes clearly reflects the theoretical ACI signal: aerosols increase N_d while reducing droplet size,
361 which in turn lowers precipitation probability and thereby increases LWP and CF. Quantitatively,
362 however, ACI intensities vary depending on the meteorological background (to be discussed in detail in
363 the following section).

364 **3.3 The Twomey Effect across the Three Periods**

365 Twomey (1977) proposed that atmospheric aerosol particles can act as cloud condensation nuclei, such
366 that an increase in aerosol loading leads to a higher cloud droplet number concentration. Under a nearly
367 constant liquid water content, this results in smaller cloud droplet effective radius. To examine the
368 Twomey effect during the three periods, the 25th and 75th percentiles of the AI were used to define clean
369 ($AI < 25$ th percentile) and polluted ($AI > 75$ th percentile) conditions, respectively. For each condition,
370 two-dimensional probability density distributions were calculated as a function of CER and LWP. The
371 difference in the two-dimensional probability densities between polluted and clean conditions therefore
372 illustrates how CER varies with aerosol loading under quasi-constant LWP. As shown in Fig. 7, CER is
373 mostly smaller $15\mu\text{m}$, justifying the effectiveness of the filtering of non-raining cases. Under clean
374 conditions, the CER of warm cloud increases with LWP across all three periods. Under polluted
375 conditions, however, CER initially increases with LWP and then tends to level off during the SW period
376 and the NEMW period. During the NEMD period, CER exhibits an increase followed by a decrease with
377 increasing LWP, and subsequently remains nearly constant. The difference plots between polluted and
378 clean conditions clearly demonstrate that polluted samples are more concentrated toward smaller CER
379 values compared with clean samples in each quasi-constant LWP bin. This consistent shift toward
380 smaller droplet sizes under higher aerosol loading demonstrates a clear manifestation of the Twomey
381 effect during all three periods.



382

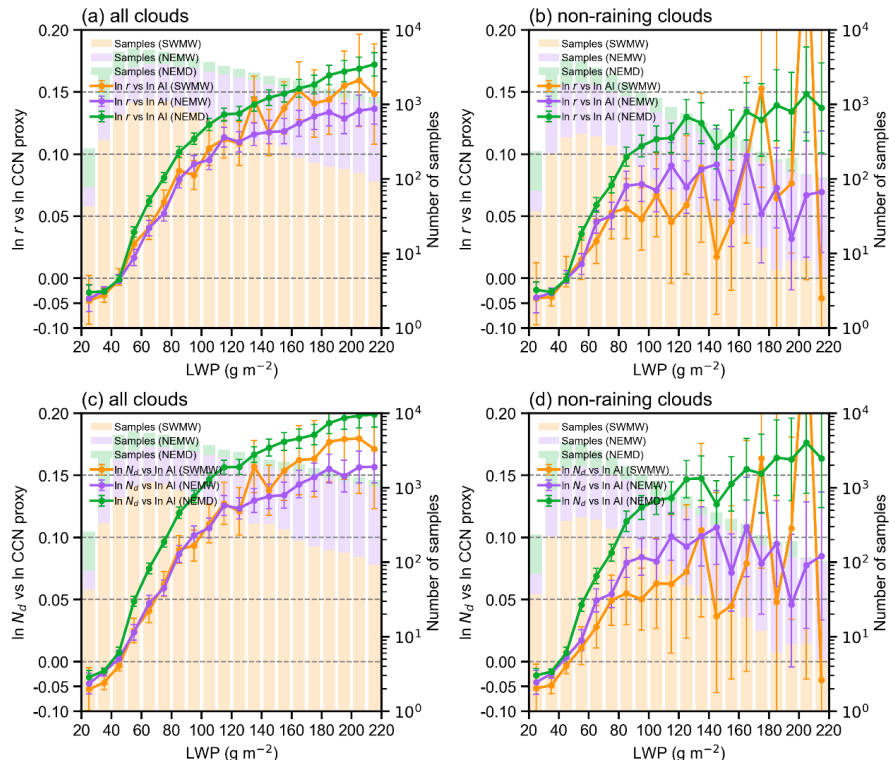
383 **Figure 7:** Joint probability distributions of liquid water path (LWP) and cloud droplet effective radius (CER)
384 for warm clouds over the South China Sea during the three periods. The first, second, and third rows
385 correspond to the southwest monsoon, the northeast monsoon wet period, and the northeast monsoon dry
386 period, respectively. The first and second columns represent clean and polluted conditions, respectively. The
387 black lines denote the mean CER values within each LWP interval. The third column shows the differences
388 in probability density between polluted and clean conditions.

389 **3.4 Variations of ACI across the Three Periods**

390 According to the assumption of the Twomey effect (Twomey, 1977), an essential prerequisite for
391 investigating the aerosol indirect effect based on the CER–AI relationship is to keep the LWP constant.
392 Since CER is a function of both LWP and AI, and generally increases with LWP, variations in LWP
393 associated with changes in aerosols can in turn modulate the CER–AI relationship. Therefore, when
394 applying the CER–AI relationship to analyse the first aerosol indirect effect, it is essential to constrain
395 LWP to ensure its constancy. To satisfy this requirement while maintaining sufficient sample sizes, LWP
396 was binned at 10 g m^{-2} intervals, within which ACI_r was examined for the three periods (Fig. 8a–b).
397 Under both all warm cloud conditions and non-raining warm cloud conditions, the anti-Twomey effect
398 (increase in CER with aerosol loading) is observed across all three periods in the SCS when $\text{LWP} < 50$
399 g m^{-2} . Clouds in this LWP regime are typically very thin or broken, as well as post-precipitation remnants



400 (McComiskey et al., 2009). A similar phenomenon is observed over the northern Indian Ocean, which
 401 may be attributed to the intense competition for available water vapor under high aerosol concentrations,
 402 combined with the entrainment of dry air at cloud tops (Jose et al., 2020). When $LWP > 50 \text{ g m}^{-2}$, the
 403 ACI for both all warm clouds and non-raining warm clouds across the three periods are consistent with
 404 the Twomey effect. An exception occurs in Fig. 8b and Fig. 8d, where the ACI at $LWP = 220 \text{ g m}^{-2}$
 405 during the southwest monsoon is negative. however, this result is not statistically robust due to the limited
 406 sample size.



407
 408 **Figure 8:** Linear regression slopes of $\ln CER$ versus $\ln AI$ (a, b) and $\ln N_d$ versus $\ln AI$ (c, d) for all warm
 409 clouds (a, c) and non-raining warm clouds (b, d) during the three periods. Green, purple, and yellow lines
 410 represent the southwest monsoon, northeast monsoon wet period, and northeast monsoon dry period,
 411 respectively. Error bars denote the 95 % confidence intervals of the linear regressions. Colored bars,
 412 consistent with the line colors, indicate the total number of samples within each LWP bin for the
 413 corresponding periods.

414 Precipitation formation efficiently reduces cloud droplet number concentration and scavenges aerosols
 415 from clouds(Gryspeerdt et al., 2015), introducing a sink of that does not reflect the Twomey effect(Jia et



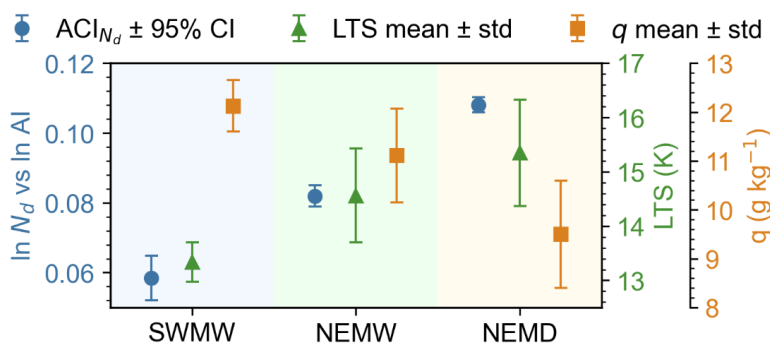
416 al., 2022). Therefore, when analyzing the aerosol first indirect effect in warm clouds, the influence of
417 precipitation should be separated in order to accurately quantify the sensitivity of CER to aerosols. Fig.
418 8 shows that, in the SCS, the ACI_r values for all warm clouds are consistently larger than those for non-
419 raining warm clouds across all three periods when LWP exceeds approximately 80 g m^{-2} . This indicates
420 that the inclusion of raining samples amplifies ACI_r , a phenomenon also identified in the AI/AOD- Na
421 relationship by Jia et al. (2022) and Painemal et al. (2020). But this amplification is just an artifact
422 governed by the joint impacts of the suppression of precipitation by aerosols and the aerosol removal by
423 precipitation (Jia et al., 2022). Therefore, after removing precipitating clouds from all warm-cloud
424 samples, the ACI_r obtained from non-raining warm clouds provides a more realistic representation.
425 Fig. 8b. shows that, under non-raining warm-cloud conditions with $LWP > 50 \text{ g m}^{-2}$, the ACI_r over the
426 SCS differs among the three periods, being largest during the NEMD period, followed by the NEMW
427 period, and smallest during the southwest monsoon. For $LWP > 160 \text{ g m}^{-2}$, the ACI_r during the southwest
428 monsoon exhibits large fluctuations due to the limited number of samples, even exceeding that of the
429 northeast monsoon. The analysis in Section 3.2 reveals substantial differences in atmospheric conditions
430 over the SCS among the three periods. During the SWMW period, atmospheric moisture and sea surface
431 temperatures reach their highest levels, and upward motion dominates over the region, while aerosol
432 concentrations remain relatively low. During the NEMW period, moisture and sea surface temperatures
433 are still relatively high, with upward motion primarily confined to the southern areas near the equator,
434 and aerosol concentrations are elevated due to pollution transported from continental China. In contrast,
435 during the NEMD period, atmospheric moisture and sea surface temperatures are at their lowest,
436 subsidence dominates, and aerosol concentrations reach their maximum. Under these distinct
437 atmospheric conditions, warm-cloud ACI over the SCS weaken progressively from the NEMW period
438 to the NEMD period and further to the southwest monsoon.
439 In addition to the radius-based ACI_r , we further examined the droplet-number susceptibility (ACI_{Nd} , Fig.
440 8c-d). Consistent with the ACI_r results, ACI_{Nd} also increases progressively from the SWMW to the
441 NEMW and further to the NEMD period, indicating that the strengthening of ACI across the three periods
442 is robust across both microphysical metrics. Such consistency highlights that the observed period-to-
443 period differences in ACI are governed by systematic changes in the underlying meteorological



444 environment rather than by the choice of ACI metric. Motivated by this consistency, Section 3.5
445 investigates how variations in moisture and LTS regulate the evolution of ACI across the three periods.

446 **3.5 Causes of ACI Variations across the Three Periods**

447 To provide an integrated view of how the ACI co-varies with the thermodynamic and moisture
448 background across the three periods, Fig. 9 shows the ACI_{Nd} together with the corresponding q and LTS.
449 Both ACI_{Nd} and the key environmental regulators display a coherent evolution across the three periods.
450 From the SWMW to the NEMW and NEMD, ACI_{Nd} intensify steadily, in parallel with declining moisture
451 and increasing LTS. Quantitatively, The ACI_{Nd} increases progressively from 0.058 ± 0.006 (95%
452 confidence interval, 95% CI) during the SWMW period to 0.082 ± 0.003 during NEMW and further to
453 0.108 ± 0.002 during NEMD. Meanwhile, q decreases from $12.126 \pm 0.526 \text{ g kg}^{-1}$ during SWMW to
454 $11.113 \pm 0.961 \text{ g kg}^{-1}$ during NEMW and $9.500 \pm 1.100 \text{ g kg}^{-1}$ during NEMD, while the LTS increases
455 from $13.338 \pm 0.361 \text{ K}$ to $14.566 \pm 0.862 \text{ K}$ and $15.349 \pm 0.980 \text{ K}$, respectively. (All q and LTS
456 uncertainties represent one standard deviation, std.) These co-varying changes indicate that both q and
457 LTS regulate the strengthening of ACI across the three periods over the SCS. In the following subsections,
458 we separately examine the roles of q (Section 3.5.1) and LTS (Section 3.5.2) in regulating ACI.



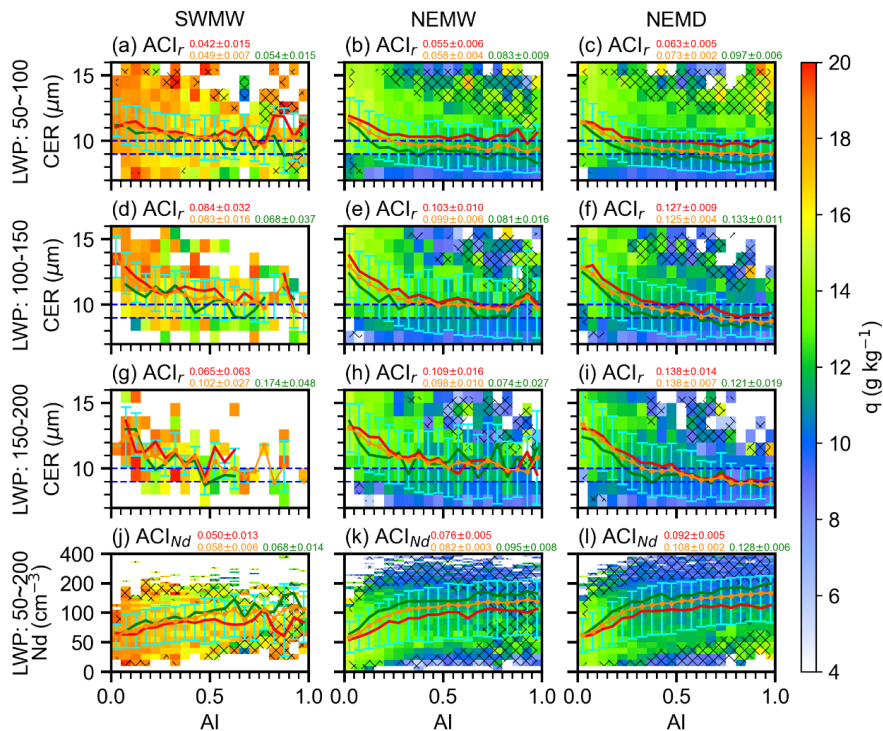
459
460 **Figure 9: ACI_{Nd} , specific humidity (q), and lower-tropospheric stability (LTS) for the three periods over the**
461 **South China Sea. The 95% confidence interval (CI) represents the uncertainty derived from the Student's t**
462 **test, whereas std denotes the one standard deviation.**

463 **3.5.1 Water vapor**

464 Water vapor supply substantially impacts CCN activation, droplet condensational growth, and
465 coalescence, hence altering the cloud droplet size distribution (Feingold et al., 2006; Zheng et al., 2022).



466 Specific humidity at 1000 hPa serves as a proxy for the ambient water vapor available to warm clouds,
467 analogous to the use of near-surface specific humidity as a proxy for marine boundary layer moisture in
468 previous studies (Dadashazar et al., 2020). To investigate the influence of water vapor on ACI, specific
469 humidity was averaged within each AI-CER/N_d interval separately for each period (Fig. 10). For each
470 AI interval, CER/N_d was further averaged, and samples were stratified by the 25th and 75th percentiles
471 of specific humidity to represent dry (< 25th percentile) and moist (> 75th percentile) conditions, under
472 which the corresponding mean CER/N_d was calculated. In addition, ACI was derived from all samples
473 and separately for the dry and moist subsets in each period. To satisfy the LWP constraint required for
474 the CER–AI analysis, the influence of water vapor on ACI was examined within LWP intervals of 50–
475 100, 100–150, and 150–200 g m⁻². In addition, because the N_d–AI relationship does not require an
476 explicit LWP constraint for ACI_{Nd} calculation, it was examined over the broader LWP range of 50–200
477 g m⁻².



478

479 **Figure 10: Influence of water vapor on ACI across the three periods. Rows 1–3 show mean specific humidity**
480 **in CER–AI bins for LWP ranges of 50–100, 100–150, and 150–200 g m⁻², respectively; row 4 shows mean**



481 specific humidity in N_d -AI bins for LWP 50–200 g m^{-2} . Columns correspond to the southwest monsoon,
482 northeast monsoon wet period, and northeast monsoon dry period. Yellow dashed, red, and green lines denote
483 the mean CER (rows 1–3) or N_d (row 4) in each AI bin for all samples, for moist conditions (specific humidity >
484 75th percentile), and for dry conditions (specific humidity < 25th percentile), respectively. Error bars indicate
485 the standard deviation of CER (rows 1–3) or N_d (row 4) within each AI bin. Yellow numbers indicate $\text{ACI} \pm$
486 95% uncertainty estimates (according to a Student's t test) for all samples, whereas red and green numbers
487 indicate the corresponding estimates under moist and dry conditions, respectively.

488 As shown in Fig. 10, higher specific humidity conditions are generally associated with larger CER and
489 lower N_d across the three periods over the SCS. This may suggest that abundant water vapor enhances
490 condensational growth of cloud droplets, and the enlarged droplets are more susceptible to collision -
491 coalescence, which not only reduces N_d but also further increases the CER. By contrast, under limited
492 water vapor availability, the ability of CCN-activated droplets to grow by condensation is substantially
493 constrained. The lack of a sufficient number of larger droplets favors condensation as the predominant
494 growth mechanism, thereby yielding smaller droplet sizes (Zheng et al., 2022).

495 The response of ACI to environmental water availability exhibits different behaviors. Qiu et al. (2017)
496 analysed the AI-CER relationship for non-raining warm clouds over the Southern Great Plains and found
497 the anti-Twomey effect under moist conditions. Zheng et al. (2022) investigated non-raining warm
498 clouds over the Eastern North Atlantic and found that sufficient water vapor availability can enhance
499 ACI. Over the SCS, within the LWP range of 50–200 g m^{-2} , ACI_{N_d} is consistently smaller under moist
500 conditions than under dry conditions across all three periods (Figs. 10j–l), suggesting that N_d exhibits
501 weaker sensitivity to aerosol perturbations in moist environments compared to dry environments. Figs.
502 10j–l show that N_d exhibits comparable values between moist and dry conditions at very low aerosol
503 loading. As aerosol concentration increases, however, N_d becomes smaller under moist conditions
504 relative to dry conditions. This pattern may indicate that under ample water vapor availability, increased
505 aerosol loading initially enhances cloud droplet activation, leading to elevated droplet number
506 concentrations. But subsequent collision-coalescence promotes droplet growth while reducing N_d .
507 Consequently, the microphysical adjustments associated with enhanced moisture availability dampen the
508 sensitivities of N_d to aerosol perturbations, manifesting as weaker ACI_{N_d} in the moist regime.

509 In contrast, the response of ACI_r to moisture exhibits a dependence on LWP. At low LWP (50–100 g m^{-2}),
510 ACI_r is reduced under moist relative to dry conditions across all periods (Figs. 10a–c). At higher LWP



511 ranges, this reduction appears only in the southwest monsoon period within the 150–200 g m⁻² range (Fig.
512 10g), whereas the opposite response holds for the other cases. The LWP is defined as the column-
513 integrated liquid water content within clouds (e.g., existing cloud droplets) (Lee and Penner, 2011). At
514 low LWP, ACI_r is weaker under moist conditions (as indicated by 1000-hPa specific humidity) compared
515 to dry conditions (Figs. 10a–c). A possible explanation is that in moist environments, enhanced collision-
516 coalescence processes promote droplet growth, leading to larger CER. In contrast, under drier conditions,
517 limited water vapor availability inhibits droplet growth, resulting in smaller CER. At higher LWP, when
518 the in-cloud liquid water content is abundant, the response of ACI_r to environmental water vapor
519 variations becomes less consistent (Figs. 10d–i), suggesting the involvement of additional microphysical
520 or dynamical processes.

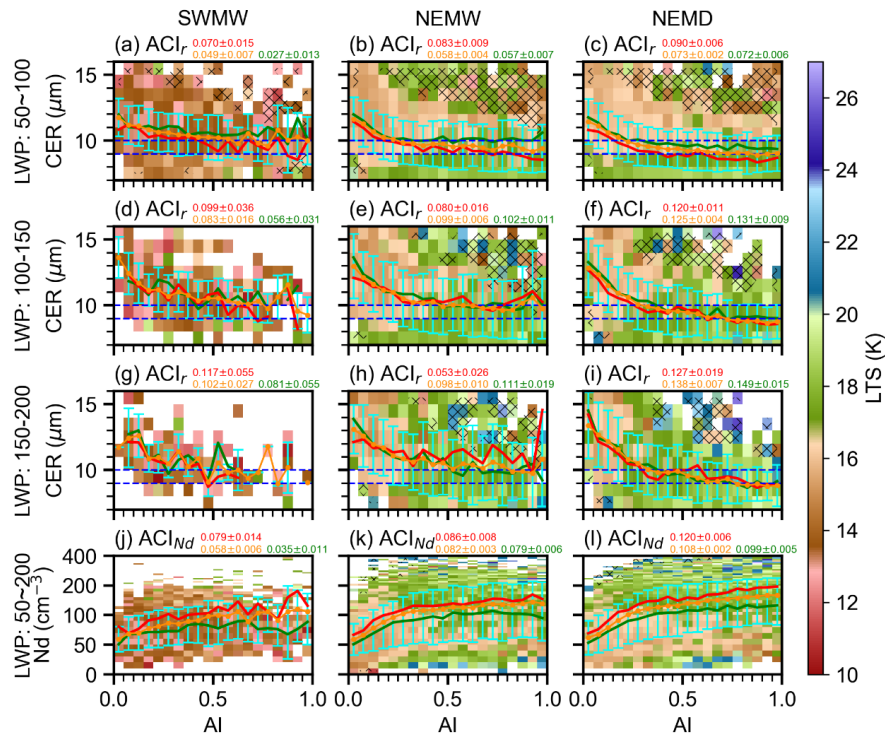
521 Over the SCS, CER and Nd exhibit comparable values across the three periods within the same LWP
522 interval at low AI. As AI increases, noticeable differences develop, with CER decreasing progressively
523 from the SW to the NEMW and further to the NEMD, while Nd increases accordingly (Fig. 10).
524 Consequently, ACI is enhanced stepwise from SW to NEMW and then to NEMD. This stepwise
525 enhancement may be partly attributed to the progressive decrease in environmental water vapor from
526 SW to NEMW and further to NEMD (Figs. 4a–c), particularly evident within the LWP interval of 50–
527 100 g m⁻².

528 **3.5.2 lower tropospheric stability**

529 Thermodynamic and dynamic conditions are key factors influencing aerosol vertical transport, aerosol
530 activation processes, and cloud droplet formation. Thermodynamic stability can be quantitatively
531 represented by the lower tropospheric stability (LTS), a measure of temperature inversion strength
532 initially defined for marine stratocumulus clouds (Klein and Hartmann, 1993). This metric has been
533 widely utilized to evaluate atmospheric stability and vertical mixing across both oceanic and continental
534 regions (Jia et al., 2019; Ma et al., 2018b). Higher LTS values represent enhanced lower tropospheric
535 stability, which suppresses vertical mixing and convective initiation. To further examine the influence of
536 thermodynamic conditions on ACI, the LTS was analysed in a manner identical to that used for specific
537 humidity. For each period, samples were stratified by the 25th and 75th percentiles of LTS to represent
538 unstable and stable conditions, respectively, and ACI was computed for each subset (Fig. 11). The



539 analysis was performed within LWP intervals of 50–100, 100–150, and 150–200 g m⁻² for the CER–AI
540 relationship, and over 50–200 g m⁻² for the Nd–AI relationship. Fig. 11 shows that stronger lower
541 tropospheric stability (higher LTS) is associated with smaller CER and higher Nd, as enhanced static
542 stability may suppresses convective mixing and vertical moisture transport, thereby limiting droplet
543 growth while favoring higher droplet concentrations.



544
545 **Figure 11:** Same as Fig. 10, but for lower tropospheric stability. Stable and unstable conditions correspond to
546 the upper (> 75th percentile) and lower (< 25th percentile) quartiles of LTS, respectively. Yellow numbers
547 indicate $ACI \pm 95\%$ uncertainty estimates (according to a Student's t test) for all samples, whereas red and
548 green numbers indicate the corresponding estimates under stable and unstable conditions, respectively.

549 In contrast to unstable conditions, stronger ACI_{Nd} is observed under stable conditions characterized by
550 higher LTS values (Figs. 11j–l). This result suggests that enhanced LTS may facilitate aerosol
551 accumulation and coagulation, leading to an increase in aerosol particle size. Larger particles are more
552 efficient on acting as CCN, thereby promoting cloud droplet activation and formation. The suppressed
553 vertical mixing associated with stable stratification may further confine aerosols and moisture within the
554 boundary layer, strengthening local ACI. Consequently, the sensitivity of Nd to aerosol perturbations is



555 enhanced under stable conditions, manifesting as higher ACI_{Nd} relative to unstable environments. Over
556 the SCS, LTS is generally weaker during the southwest monsoon than during the northeast monsoon (Fig.
557 11). The stronger atmospheric stability associated with the northeast monsoon favors enhanced ACI in
558 warm clouds, resulting in stronger ACI during the NE compared with the SW.
559 The response of ACI_r to LTS exhibits distinct behaviors across different LWP intervals and periods (Figs.
560 11a–i). During the southwest monsoon period, ACI_r is consistently larger under stable conditions than
561 under unstable conditions across all three LWP ranges, consistent with the ACI_{Nd} results. However,
562 during the NEMW and NEMD periods, such an enhancement is only evident within the lowest LWP
563 interval (50–100 $g\ m^{-2}$). At higher LWP ranges (100–150 and 150–200 $g\ m^{-2}$), ACI_r becomes smaller
564 under stable conditions relative to unstable ones. This contrasting behavior (Figs. 11e, f, h, i) can be
565 further understood from the AI-CER relationships. At low AI values, corresponding to relatively clean
566 conditions, CER is larger under unstable conditions than under stable conditions. As AI increases,
567 indicating more polluted environments, CER under stable and unstable conditions gradually converges,
568 leading to stronger ACI_r under unstable conditions. This pattern may indicate that during the northeast
569 monsoon period, when in-cloud water vapor is abundant and aerosol loading is relatively high, cloud
570 microphysical processes become less sensitive to variations in LTS. The inherently strong and weakly
571 variable lower-tropospheric stability during the northeast monsoon may suppress the dynamical
572 influence of further LTS changes ACI, thereby weakening the LTS dependence of ACI_r under moist and
573 polluted conditions.

574 **4 Conclusions**

575 To investigate how ACI vary under the alternating influence of two opposing monsoon systems over the
576 South China Sea (SCS) and how different environmental conditions modulate these interactions, the
577 study period was divided into three representative phases based on variations in wind direction,
578 precipitation, and specific humidity: the southwest monsoon (SW), the northeast monsoon wet period
579 (NEMW), and the northeast monsoon dry period (NEMD). By integrating reanalysis data and satellite
580 observations, this study examined the variations in ACI and the associated environmental controlling
581 factors during these three periods. The main findings are summarized as follows:



582 1. SCS exhibits distinct seasonal environmental conditions associated with the prevailing monsoon
583 regimes. During the SW, the SCS is dominated by strong upward motion, high SSTs, and abundant
584 atmospheric moisture. During the NEMW, continental outflow transports aerosols over the SCS while
585 SSTs decrease and LTS strengthens; ascent is largely confined to the equatorial south and moisture
586 remains relatively high. During the NEMD, continental influence persists but the environment becomes
587 drier and more stable, with the lowest SSTs and widespread subsidence, favoring the boundary-layer
588 accumulation of fine-mode aerosols. These contrasting meteorological and environmental conditions
589 among the SW, NEMW, and NEMD periods establish a distinct seasonal background over the SCS and
590 exert a decisive influence on ACI.

591 2. A pronounced Twomey effect was consistently identified across all three periods, as indicated by
592 smaller CER and higher Nd with increasing aerosol loading under nearly constant LWP. Quantitative
593 estimates of ACI_r show that the Twomey effect dominates when LWP exceeds 50 g m^{-2} , whereas an
594 apparent “anti-Twomey” behavior appears in optically thin clouds ($LWP < 50 \text{ g m}^{-2}$), likely associated
595 with strong competition for limited water vapor and entrainment-induced drying. Precipitation tends to
596 amplify the ACI by simultaneously suppressing cloud droplet number concentrations and removing
597 aerosols from the atmosphere. After removing raining samples, the ACI derived from non-raining warm
598 clouds provides a more reliable representation of the first aerosol indirect effect, reducing biases caused
599 by precipitation processes. Among the three periods, ACI is smallest during the SW, increases during
600 the NEMW, and reaches its maximum during the NEMD.

601 3. Environmental conditions exert a strong influence on ACI intensity over the SCS. Water vapor
602 availability plays a critical role in regulating cloud droplet activation and growth. ACI_{Nd} is consistently
603 smaller under moist conditions than under dry conditions across all three periods, indicating that Nd
604 exhibits weaker sensitivity to aerosol perturbations in moist environments compared to dry environments.
605 Thermodynamic stability also modulates ACI variability. ACI_{Nd} is generally enhanced under stable
606 atmospheric conditions, as stronger LTS may suppress vertical mixing and confine aerosols and moisture
607 within the boundary layer, thereby facilitating aerosol accumulation and potentially promoting CCN
608 activation. Overall, ACI is most pronounced in dry and stable environments, which are typical of the
609 NEMD, and weakest under moist and convectively active environments during the SW.



610 Overall, the strength of ACI over the SCS increases progressively from the SW to NEMW and further to
611 NEMD, primarily driven by decreasing moisture availability and increasing atmospheric stability. These
612 results highlight that the coupling among aerosols, moisture, and thermodynamic stability exerts
613 fundamental control over marine warm-cloud microphysical processes in tropical monsoon regions. The
614 findings provide important observational evidence for understanding ACI and offer valuable guidance
615 for improving the representation of ACI in climate and numerical weather prediction models.

616

617 Financial support

618 This work was supported by the National Natural Science Foundation of China (grant nos. 42027804,
619 41775026, and 41075012). Hailing Jia was support by the project ACIaction (File No.
620 OCENW.M.24.024) financed by the Dutch Research Council (NWO) under the grant
621 <https://doi.org/10.61686/OZRJI30024>.

622

623 Acknowledgements

624 Data and samples were collected onboard of R/V Shiyan 6 implementing the open research cruise
625 NORC2024-07 supported by NSFC Shiptime Sharing Project (project number: 42349907).

626

627 Competing Interest

628 The authors declare that they have no known competing financial interests or personal relationships that
629 could have appeared to influence the work reported in this paper.

630

631 Author contributions

632 YL analysed the data and wrote the manuscript. HJ and YH participated in scientific discussions and
633 reviewed and refined the manuscript.

634

635 Data Availability



636 Atmospheric fields were obtained from the ERA5 reanalysis datasets produced by the European Centre
637 for Medium-Range Weather Forecasts (ECMWF) via the Copernicus Climate Change Service (C3S)
638 Climate Data Store (CDS). The data are publicly available at <https://cds.climate.copernicus.eu/>.
639 Aerosol datasets were obtained from the Modern-Era Retrospective Analysis for Research and
640 Applications Version 2 (MERRA-2), produced by the NASA Goddard Earth Observing System (GEOS)
641 Global Modeling and Assimilation Office (GMAO) and distributed by the Goddard Earth Sciences Data
642 and Information Services Center (GES DISC). The data are publicly available at
643 <https://disc.gsfc.nasa.gov/datasets?project=MERRA-2>.
644 Cloud retrievals were obtained from the Clouds and the Earth's Radiant Energy System (CERES)-
645 Moderate Resolution Imaging Spectroradiometer (MODIS) Edition 4 Single Scanner Footprint (SSF)
646 daily Level-3 products ($1^\circ \times 1^\circ$ grid), produced by NASA's Langley Research Center (LaRC) and
647 distributed by the Atmospheric Science Data Center (ASDC). The CERES-MODIS data are publicly
648 available through the NASA ASDC archive at <https://ceres.larc.nasa.gov/data/#ssf1deg-level-3>.
649 Sea surface temperature (SST) data were obtained from the National Oceanic and Atmospheric
650 Administration (NOAA) Optimum Interpolation (OI) SST, Version 2, produced by the NOAA Physical
651 Sciences Laboratory. The data are publicly available through the NOAA Physical Sciences Laboratory
652 at <https://psl.noaa.gov/data/gridded/data.noaa.oisst.v2.html>.
653 IMERG V07 precipitation data used in this study are openly available from the NASA Goddard Earth
654 Sciences Data and Information Services Center (GES DISC) at
655 <https://disc.gsfc.nasa.gov/datasets?keywords=gpm%20imerg%2007>, as cited in Huffman et al. (2024).
656

657 **References**

658 Ackerman, A. S., Kirkpatrick, M. P., Stevens, D. E., and Toon, O. B.: The impact of humidity above
659 stratiform clouds on indirect aerosol climate forcing, *Nature*, 432, 1014–1017,
660 <https://doi.org/10.1038/nature03174>, 2004.
661 Albrecht, B. A.: Aerosols, Cloud Microphysics, and Fractional Cloudiness, *Science*, 245, 1227–1230,
662 1989.



663 Bellouin, N., Quaas, J., Gryspeerdt, E., Kinne, S., Stier, P., Watson-Parris, D., Boucher, O., Carslaw, K.
664 S., Christensen, M., Daniau, A.-L., Dufresne, J.-L., Feingold, G., Fiedler, S., Forster, P., Gettelman, A.,
665 Haywood, J. M., Lohmann, U., Malavelle, F., Mauritzen, T., McCoy, D. T., Myhre, G., Mülmenstädt, J.,
666 Neubauer, D., Possner, A., Rugenstein, M., Sato, Y., Schulz, M., Schwartz, S. E., Sourdeval, O.,
667 Storelvmo, T., Toll, V., Winker, D., and Stevens, B.: Bounding Global Aerosol Radiative Forcing of
668 Climate Change, *Reviews of Geophysics*, 58, e2019RG000660, <https://doi.org/10.1029/2019RG000660>,
669 2020.

670 Braun, R. A., Dadashazar, H., MacDonald, A. B., Crosbie, E., Jonsson, H. H., Woods, R. K., Flagan, R.
671 C., Seinfeld, J. H., and Sorooshian, A.: Cloud Adiabaticity and Its Relationship to Marine Stratocumulus
672 Characteristics Over the Northeast Pacific Ocean, *Journal of Geophysical Research: Atmospheres*, 123,
673 13,790–13,806, <https://doi.org/10.1029/2018JD029287>, 2018.

674 Chen, J. and Hu, Z.: Seasonal variability in spatial patterns of sea surface cold- and warm fronts over the
675 continental shelf of the northern South China Sea, *Front. Mar. Sci.*, 9,
676 <https://doi.org/10.3389/fmars.2022.1100772>, 2023.

677 Chen, Y., Luo, T., Sun, G., Zhu, W., Liu, Q., Liu, Y., Jin, X., and Weng, N.: A Comprehensive Ensemble
678 Model for Marine Atmospheric Boundary-Layer Prediction in Meteorologically Sparse and Complex
679 Regions: A Case Study in the South China Sea, *Remote Sensing*, 17, 2046,
680 <https://doi.org/10.3390/rs17122046>, 2025.

681 Chen, Y.-C., Christensen, M. W., Stephens, G. L., and Seinfeld, J. H.: Satellite-based estimate of global
682 aerosol-cloud radiative forcing by marine warm clouds, *Nature Geosci.*, 7, 643–646,
683 <https://doi.org/10.1038/ngeo2214>, 2014.

684 Costantino, L. and Bréon, F.-M.: Aerosol indirect effect on warm clouds over South-East Atlantic, from
685 co-located MODIS and CALIPSO observations, *Atmospheric Chemistry and Physics*, 13, 69–88,
686 <https://doi.org/10.5194/acp-13-69-2013>, 2013.

687 Dadashazar, H., Crosbie, E., Majdi, M. S., Panahi, M., Moghaddam, M. A., Behrangi, A., Brunke, M.,
688 Zeng, X., Jonsson, H. H., and Sorooshian, A.: Stratocumulus cloud clearings: statistics from satellites,
689 reanalysis models, and airborne measurements, *Atmos. Chem. Phys.*, 20, 4637–4665,
690 <https://doi.org/10.5194/acp-20-4637-2020>, 2020.

691 Dadashazar, H., Painemal, D., Alipanah, M., Brunke, M., Chellappan, S., Corral, A. F., Crosbie, E.,
692 Kirschler, S., Liu, H., Moore, R. H., Robinson, C., Scarino, A. J., Shook, M., Sinclair, K., Thomhill, K.
693 L., Voigt, C., Wang, H., Winstead, E., Zeng, X., Ziembka, L., Zuidema, P., and Sorooshian, A.: Cloud
694 drop number concentrations over the western North Atlantic Ocean: seasonal cycle, aerosol
695 interrelationships, and other influential factors, *Atmos. Chem. Phys.*, 21, 10499–10526,
696 <https://doi.org/10.5194/acp-21-10499-2021>, 2021.

697 Dagan, G., Koren, I., Altaratz, O., and Heiblum, R. H.: Time-dependent, non-monotonic response of
698 warm convective cloud fields to changes in aerosol loading, *Atmospheric Chemistry and Physics*, 17,
699 7435–7444, <https://doi.org/10.5194/acp-17-7435-2017>, 2017.



700 Dezfuli, A. K., Ichoku, C. M., Huffman, G. J., Mohr, K. I., Selker, J. S., Van De Giesen, N., Hochreutener,
701 R., and Annor, F. O.: Validation of IMERG Precipitation in Africa, *Journal of Hydrometeorology*, 18,
702 2817–2825, <https://doi.org/10.1175/JHM-D-17-0139.1>, 2017.

703 Douglas, A. and L'Ecuyer, T.: Quantifying variations in shortwave aerosol–cloud–radiation interactions
704 using local meteorology and cloud state constraints, *Atmospheric Chemistry and Physics*, 19, 6251–6268,
705 <https://doi.org/10.5194/acp-19-6251-2019>, 2019.

706 Douville, H., Raghavan, K., Renwick, J., Allan, R. P., Arias, P. A., Barlow, M., Cerezo-Mota, R., Cherchi,
707 A., Gan, T. Y., and Gergis, J.: Climate Change 2021 – The Physical Science Basis: Working Group I
708 Contribution to the Sixth Assessment Report of the Intergovernmental Panel on Climate Change, 1st ed.,
709 Cambridge University Press, <https://doi.org/10.1017/9781009157896>, 2023.

710 Durden, S. L.: Evaluation of IMERG Data over Open Ocean Using Observations of Tropical Cyclones,
711 *Remote Sensing*, 16, 2028, <https://doi.org/10.3390/rs16112028>, 2024.

712 Fan, J., Yuan, T., Comstock, J. M., Ghan, S., Khain, A., Leung, L. R., Li, Z., Martins, V. J., and
713 Ovchinnikov, M.: Dominant role by vertical wind shear in regulating aerosol effects on deep convective
714 clouds, *Journal of Geophysical Research: Atmospheres*, 114, <https://doi.org/10.1029/2009JD012352>,
715 2009.

716 Fan, J., Wang, Y., Rosenfeld, D., and Liu, X.: Review of Aerosol–Cloud Interactions: Mechanisms,
717 Significance, and Challenges, <https://doi.org/10.1175/JAS-D-16-0037.1>, 2016.

718 Feingold, G., Remer, L. A., Ramaprasad, J., and Kaufman, Y. J.: Analysis of smoke impact on clouds in
719 Brazilian biomass burning regions: An extension of Twomey's approach, *J. Geophys. Res.*, 106, 22907–
720 22922, <https://doi.org/10.1029/2001JD000732>, 2001.

721 Feingold, G., Furrer, R., Pilewskie, P., Remer, L. A., Min, Q., and Jonsson, H.: Aerosol indirect effect
722 studies at Southern Great Plains during the May 2003 Intensive Operations Period, *Journal of
723 Geophysical Research: Atmospheres*, 111, <https://doi.org/10.1029/2004JD005648>, 2006.

724 Gelaro, R., McCarty, W., Suárez, M. J., Todling, R., Molod, A., Takacs, L., Randles, C. A., Darmenov,
725 A., Bosilovich, M. G., Reichle, R., Wargan, K., Coy, L., Cullather, R., Draper, C., Akella, S., Buchard,
726 V., Conaty, A., Silva, A. M. da, Gu, W., Kim, G.-K., Koster, R., Lucchesi, R., Merkova, D., Nielsen, J.
727 E., Partyka, G., Pawson, S., Putman, W., Rienecker, M., Schubert, S. D., Sienkiewicz, M., and Zhao, B.:
728 The Modern-Era Retrospective Analysis for Research and Applications, Version 2 (MERRA-2),
729 <https://doi.org/10.1175/JCLI-D-16-0758.1>, 2017.

730 Grosvenor, D. P., Sourdeval, O., Zuidema, P., Ackerman, A., Alexandrov, M. D., Bennartz, R., Boers,
731 R., Cairns, B., Chiu, J. C., Christensen, M., Deneke, H., Diamond, M., Feingold, G., Fridlind, A.,
732 Hünerbein, A., Knist, C., Kollias, P., Marshak, A., McCoy, D., Merk, D., Painemal, D., Rausch, J.,
733 Rosenfeld, D., Russchenberg, H., Seifert, P., Sinclair, K., Stier, P., van Diedenhoven, B., Wendisch, M.,
734 Werner, F., Wood, R., Zhang, Z., and Quaas, J.: Remote Sensing of Droplet Number Concentration in



735 Warm Clouds: A Review of the Current State of Knowledge and Perspectives, *Reviews of Geophysics*,
736 56, 409–453, <https://doi.org/10.1029/2017RG000593>, 2018.

737 Gryspeerdt, E., Stier, P., White, B. A., and Kipling, Z.: Wet scavenging limits the detection of aerosol
738 effects on precipitation, *Atmospheric Chemistry and Physics*, 15, 7557–7570,
739 <https://doi.org/10.5194/acp-15-7557-2015>, 2015.

740 Gryspeerdt, E., Goren, T., Sourdeval, O., Quaas, J., Mülmenstädt, J., Dipu, S., Unglaub, C., Gettelman,
741 A., and Christensen, M.: Constraining the aerosol influence on cloud liquid water path, *Atmospheric
742 Chemistry and Physics*, 19, 5331–5347, <https://doi.org/10.5194/acp-19-5331-2019>, 2019.

743 Hayden, L. J. M., Tan, J., Bolvin, D. T., and Huffman, G. J.: Variations in the Diurnal Cycle of
744 Precipitation and Its Changes with Distance from Shore over Two Contrasting Regions as Observed by
745 IMERG, ERA5, and Spaceborne Ku Radar, *Journal of Hydrometeorology*, 24, 675–689,
746 <https://doi.org/10.1175/JHM-D-22-0154.1>, 2023.

747 Hersbach, H., Bell, B., Berrisford, P., Hirahara, S., Horányi, A., Muñoz-Sabater, J., Nicolas, J., Peubey,
748 C., Radu, R., Schepers, D., Simmons, A., Soci, C., Abdalla, S., Abellán, X., Balsamo, G., Bechtold, P.,
749 Biavati, G., Bidlot, J., Bonavita, M., De Chiara, G., Dahlgren, P., Dee, D., Diamantakis, M., Dragani, R.,
750 Flemming, J., Forbes, R., Fuentes, M., Geer, A., Haimberger, L., Healy, S., Hogan, R. J., Hólm, E.,
751 Janisková, M., Keeley, S., Laloyaux, P., Lopez, P., Lupu, C., Radnoti, G., De Rosnay, P., Rozum, I.,
752 Vamborg, F., Villaume, S., and Thépaut, J.: The ERA5 global reanalysis, *Quart J Royal Meteorol Soc*,
753 146, 1999–2049, <https://doi.org/10.1002/qj.3803>, 2020.

754 Huffman, G. J., Bolvin, D. T., Braithwaite, D., Hsu, K.-L., Joyce, R. J., Kidd, C., Nelkin, E. J.,
755 Sorooshian, S., Stocker, E. F., Tan, J., Wolff, D. B., and Xie, P.: Integrated Multi-satellite Retrievals for
756 the Global Precipitation Measurement (GPM) Mission (IMERG), in: *Satellite Precipitation Measurement*,
757 vol. 67, edited by: Levizzani, V., Kidd, C., Kirschbaum, D. B., Kummerow, C. D., Nakamura, K., and
758 Turk, F. J., Springer International Publishing, Cham, 343–353, https://doi.org/10.1007/978-3-030-24568-9_19, 2020.

760 Huffman, G. J., Bolvin, D. T., Braithwaite, D., Hsu, K., Joyce, R., Kidd, C., Nelkin, E., Sorooshian, S.,
761 Tan, J., and Xie, P.: NASA Global Precipitation Measurement (GPM) Integrated Multi-Satellite
762 Retrievals for GPM (IMERG) Version 07, *Algorithm Theoretical Basis Document (ATBD) Version*, 47,
763 2023.

764 Jia, H. and Quaas, J.: Nonlinearity of the cloud response postpones climate penalty of mitigating air
765 pollution in polluted regions, *Nat. Clim. Chang.*, 13, 943–950, <https://doi.org/10.1038/s41558-023-01775-5>, 2023.

767 Jia, H., Ma, X., Quaas, J., Yin, Y., and Qiu, T.: Is positive correlation between cloud droplet effective
768 radius and aerosol optical depth over land due to retrieval artifacts or real physical processes?, *Atmos.
769 Chem. Phys.*, 19, 8879–8896, <https://doi.org/10.5194/acp-19-8879-2019>, 2019.



770 Jia, H., Ma, X., Yu, F., and Quaas, J.: Significant underestimation of radiative forcing by aerosol–cloud
771 interactions derived from satellite-based methods, *Nat Commun*, 12, 3649,
772 <https://doi.org/10.1038/s41467-021-23888-1>, 2021.

773 Jia, H., Quaas, J., Gryspeerdt, E., Böhm, C., and Sourdeval, O.: Addressing the difficulties in quantifying
774 droplet number response to aerosol from satellite observations, *Atmospheric Chemistry and Physics*, 22,
775 7353–7372, <https://doi.org/10.5194/acp-22-7353-2022>, 2022.

776 Jose, S., Nair, V. S., and Babu, S. S.: Anthropogenic emissions from South Asia reverses the aerosol
777 indirect effect over the northern Indian Ocean, *Sci Rep*, 10, 18360, [https://doi.org/10.1038/s41598-020-74897-x](https://doi.org/10.1038/s41598-020-
778 74897-x), 2020.

779 Kim, B.-G., Schwartz, S. E., Miller, M. A., and Min, Q.: Effective radius of cloud droplets by ground-
780 based remote sensing: Relationship to aerosol, *Journal of Geophysical Research: Atmospheres*, 108,
781 <https://doi.org/10.1029/2003JD003721>, 2003.

782 Klein, S. A. and Hartmann, D. L.: The Seasonal Cycle of Low Stratiform Clouds, 1993.

783 Lee, S. S. and Penner, J. E.: Dependence of aerosol–cloud interactions in stratocumulus clouds on liquid-
784 water path, *Atmospheric Environment*, 45, 6337–6346, <https://doi.org/10.1016/j.atmosenv.2011.08.050>,
785 2011.

786 Lee, T.-W. and Park, J. E.: Thermodynamic correlations between the sea surface temperature, water
787 vapor content, and cloud fraction, using MODIS data, *Theor Appl Climatol*, 150, 1699–1706,
788 <https://doi.org/10.1007/s00704-022-04261-8>, 2022.

789 Liu, J., Yu, J., Lin, C., He, M., Liu, H., Wang, W., and Min, M.: Near-real-time atmospheric and oceanic
790 science products of Himawari-8 and Himawari-9 geostationary satellites over the South China Sea, *Earth
791 System Science Data*, 16, 4949–4969, <https://doi.org/10.5194/essd-16-4949-2024>, 2024.

792 Ma, P.-L., Rasch, P. J., Chepfer, H., Winker, D. M., and Ghan, S. J.: Observational constraint on cloud
793 susceptibility weakened by aerosol retrieval limitations, *Nat Commun*, 9, 2640,
794 <https://doi.org/10.1038/s41467-018-05028-4>, 2018a.

795 Ma, X., Jia, H., Yu, F., and Quaas, J.: Opposite Aerosol Index–Cloud Droplet Effective Radius
796 Correlations Over Major Industrial Regions and Their Adjacent Oceans, *Geophysical Research Letters*,
797 45, 5771–5778, <https://doi.org/10.1029/2018GL077562>, 2018b.

798 Martin, D. W. and Howland, M. R.: Rainfall over the Arabian Sea during the onset of the 1979 monsoon,
799 *Nature*, 300, 628–630, <https://doi.org/10.1038/300628a0>, 1982.

800 Martin, G. M., Johnson, D. W., and Spice, A.: The Measurement and Parameterization of Effective
801 Radius of Droplets in Warm Stratocumulus Clouds, 1994.



802 McComiskey, A., Feingold, G., Frisch, A. S., Turner, D. D., Miller, M. A., Chiu, J. C., Min, Q., and
803 Ogren, J. A.: An assessment of aerosol-cloud interactions in marine stratus clouds based on surface
804 remote sensing, *J. Geophys. Res.*, 114, 2008JD011006, <https://doi.org/10.1029/2008JD011006>, 2009.

805 Miller, R. M., Rauber, R. M., Di Girolamo, L., Rilloraza, M., Fu, D., McFarquhar, G. M., Nesbitt, S. W.,
806 Ziemb, L. D., Woods, S., and Thornhill, K. L.: Influence of natural and anthropogenic aerosols on cloud
807 base droplet size distributions in clouds over the South China Sea and West Pacific, *Atmospheric*
808 *Chemistry and Physics*, 23, 8959–8977, <https://doi.org/10.5194/acp-23-8959-2023>, 2023.

809 Minnis, P., Sun-Mack, S., Young, D. F., Heck, P. W., Garber, D. P., Chen, Y., Spangenberg, D. A.,
810 Arduini, R. F., Trepte, Q. Z., Smith, W. L., Ayers, J. K., Gibson, S. C., Miller, W. F., Hong, G.,
811 Chakrapani, V., Takano, Y., Liou, K.-N., Xie, Y., and Yang, P.: CERES Edition-2 Cloud Property
812 Retrievals Using TRMM VIRS and Terra and Aqua MODIS Data—Part I: Algorithms, *IEEE*
813 *Transactions on Geoscience and Remote Sensing*, 49, 4374–4400,
814 <https://doi.org/10.1109/TGRS.2011.2144601>, 2011a.

815 Minnis, P., Sun-Mack, S., Chen, Y., Khaiyer, M. M., Yi, Y., Ayers, J. K., Brown, R. R., Dong, X., Gibson,
816 S. C., Heck, P. W., Lin, B., Nordeen, M. L., Nguyen, L., Palikonda, R., Smith, W. L., Spangenberg, D.
817 A., Trepte, Q. Z., and Xi, B.: CERES Edition-2 Cloud Property Retrievals Using TRMM VIRS and Terra
818 and Aqua MODIS Data—Part II: Examples of Average Results and Comparisons With Other Data, *IEEE*
819 *Transactions on Geoscience and Remote Sensing*, 49, 4401–4430,
820 <https://doi.org/10.1109/TGRS.2011.2144602>, 2011b.

821 Minnis, P., Sun-Mack, S., Chen, Y., Chang, F.-L., Yost, C. R., Smith, W. L., Heck, P. W., Arduini, R.
822 F., Bedka, S. T., Yi, Y., Hong, G., Jin, Z., Painemal, D., Palikonda, R., Scarino, B. R., Spangenberg, D.
823 A., Smith, R. A., Trepte, Q. Z., Yang, P., and Xie, Y.: CERES MODIS Cloud Product Retrievals for
824 Edition 4—Part I: Algorithm Changes, *IEEE Transactions on Geoscience and Remote Sensing*, 59,
825 2744–2780, <https://doi.org/10.1109/TGRS.2020.3008866>, 2021.

826 Nakajima, T., Higurashi, A., Kawamoto, K., and Penner, J. E.: A possible correlation between satellite-
827 derived cloud and aerosol microphysical parameters, *Geophysical Research Letters*, 28, 1171–1174,
828 <https://doi.org/10.1029/2000GL012186>, 2001.

829 Ou, H., Cai, M., Zhang, Y., Ni, X., Liang, B., Sun, Q., Mai, S., Sun, C., Zhou, S., Wang, H., Sun, J., and
830 Zhao, J.: Measurement report: Cloud condensation nuclei (CCN) activity in the South China Sea from
831 shipborne observations during the summer and winter of 2021 – seasonal variation and anthropogenic
832 influence, *Atmospheric Chemistry and Physics*, 25, 2495–2513, <https://doi.org/10.5194/acp-25-2495-2025>, 2025.

834 Painemal, D.: Global estimates of changes in shortwave low-cloud albedo and fluxes due to variations
835 in cloud droplet number concentration derived from CERES-MODIS satellite sensors, *Geophys Res Lett*,
836 45, 9288–9296, <https://doi.org/10.1029/2018GL078880>, 2018.

837 Painemal, D., Chang, F.-L., Ferrare, R., Burton, S., Li, Z., Smith Jr., W. L., Minnis, P., Feng, Y., and
838 Clayton, M.: Reducing uncertainties in satellite estimates of aerosol–cloud interactions over the



839 subtropical ocean by integrating vertically resolved aerosol observations, *Atmospheric Chemistry and*
840 *Physics*, 20, 7167–7177, <https://doi.org/10.5194/acp-20-7167-2020>, 2020.

841 Painemal, D., Corral, A. F., Sorooshian, A., Brunke, M. A., Chellappan, S., Afzali Gorooh, V., Ham, S.-
842 H., O'Neill, L., Smith Jr., W. L., Tselioudis, G., Wang, H., Zeng, X., and Zuidema, P.: An Overview of
843 Atmospheric Features Over the Western North Atlantic Ocean and North American East Coast—Part 2:
844 Circulation, Boundary Layer, and Clouds, *Journal of Geophysical Research: Atmospheres*, 126,
845 e2020JD033423, <https://doi.org/10.1029/2020JD033423>, 2021.

846 Peng, S., Zhu, Y., Huang, K., Ding, X., Shi, R., Wu, D., Feng, Y., and Wang, D.: Detecting the structure
847 of marine atmospheric boundary layer over the Northern South China Sea by shipboard GPS sondes,
848 *Atmospheric Science Letters*, 17, 564–568, <https://doi.org/10.1002/asl.693>, 2016.

849 Qiu, Y., Zhao, C., Guo, J., and Li, J.: 8-Year ground-based observational analysis about the seasonal
850 variation of the aerosol-cloud droplet effective radius relationship at SGP site, *Atmospheric Environment*,
851 164, 139–146, <https://doi.org/10.1016/j.atmosenv.2017.06.002>, 2017.

852 Reynolds, R. W., Rayner, N. A., Smith, T. M., Stokes, D. C., and Wang, W.: An Improved In Situ and
853 Satellite SST Analysis for Climate, 2002.

854 Rosenfeld, D., Zhu, Y., Wang, M., Zheng, Y., Goren, T., and Yu, S.: Aerosol-driven droplet
855 concentrations dominate coverage and water of oceanic low-level clouds, *Science*, 363, eaav0566,
856 <https://doi.org/10.1126/science.aav0566>, 2019.

857 Saponaro, G., Kolmonen, P., Sogacheva, L., Rodriguez, E., Virtanen, T., and De Leeuw, G.: Estimates
858 of the aerosol indirect effect over the Baltic Sea region derived from 12 years of MODIS observations,
859 *Atmos. Chem. Phys.*, 17, 3133–3143, <https://doi.org/10.5194/acp-17-3133-2017>, 2017.

860 Sato, Y., Goto, D., Michibata, T., Suzuki, K., Takemura, T., Tomita, H., and Nakajima, T.: Aerosol
861 effects on cloud water amounts were successfully simulated by a global cloud-system resolving model,
862 *Nat Commun*, 9, 985, <https://doi.org/10.1038/s41467-018-03379-6>, 2018.

863 Seinfeld, J. H., Bretherton, C., Carslaw, K. S., Coe, H., DeMott, P. J., Dunlea, E. J., Feingold, G., Ghan,
864 S., Guenther, A. B., Kahn, R., Kraucunas, I., Kreidenweis, S. M., Molina, M. J., Nenes, A., Penner, J. E.,
865 Prather, K. A., Ramanathan, V., Ramaswamy, V., Rasch, P. J., Ravishankara, A. R., Rosenfeld, D.,
866 Stephens, G., and Wood, R.: Improving our fundamental understanding of the role of aerosol–cloud
867 interactions in the climate system, *Proceedings of the National Academy of Sciences*, 113, 5781–5790,
868 <https://doi.org/10.1073/pnas.1514043113>, 2016.

869 Sorooshian, A., Anderson, B., Bauer, S. E., Braun, R. A., Cairns, B., Crosbie, E., Dadashazar, H., Diskin,
870 G., Ferrare, R., Flagan, R. C., Hair, J., Hostetler, C., Jonsson, H. H., Kleb, M. M., Liu, H., McDonald,
871 A. B., McComiskey, A., Moore, R., Painemal, D., Russell, L. M., Seinfeld, J. H., Shook, M., Smith, W.
872 L., Thomhill, K., Tselioudis, G., Wang, H., Zeng, X., Zhang, B., Ziembka, L., and Zuidema, P.: Aerosol–
873 Cloud–Meteorology Interaction Airborne Field Investigations: Using Lessons Learned from the U.S.



874 West Coast in the Design of ACTIVATE off the U.S. East Coast, <https://doi.org/10.1175/BAMS-D-18-0100.1>, 2019.

875

876 Stier, P., Van Den Heever, S. C., Christensen, M. W., Gryspenert, E., Dagan, G., Saleeby, S. M.,
877 Bollasina, M., Donner, L., Emanuel, K., Ekman, A. M. L., Feingold, G., Field, P., Forster, P., Haywood,
878 J., Kahn, R., Koren, I., Kummerow, C., L'Ecuyer, T., Lohmann, U., Ming, Y., Myhre, G., Quaas, J.,
879 Rosenfeld, D., Samset, B., Seifert, A., Stephens, G., and Tao, W.-K.: Multifaceted aerosol effects on
880 precipitation, *Nat. Geosci.*, 17, 719–732, <https://doi.org/10.1038/s41561-024-01482-6>, 2024.

881 Su, W., Loeb, N. G., Xu, K.-M., Schuster, G. L., and Eitzen, Z. A.: An estimate of aerosol indirect effect
882 from satellite measurements with concurrent meteorological analysis, *Journal of Geophysical Research: Atmospheres*, 115, <https://doi.org/10.1029/2010JD013948>, 2010.

883

884 Sun, Q., Liang, B., Cai, M., Zhang, Y., Ou, H., Ni, X., Sun, X., Han, B., Deng, X., Zhou, S., and Zhao,
885 J.: Cruise observation of the marine atmosphere and ship emissions in South China Sea: Aerosol
886 composition, sources, and the aging process, *Environmental Pollution*, 316, 120539,
887 <https://doi.org/10.1016/j.envpol.2022.120539>, 2023.

888

889 Tan, J., Huffman, G. J., Bolvin, D. T., and Nelkin, E. J.: Diurnal Cycle of IMERG V06 Precipitation,
Geophysical Research Letters, 46, 13584–13592, <https://doi.org/10.1029/2019GL085395>, 2019a.

890

891 Tan, J., Huffman, G. J., Bolvin, D. T., and Nelkin, E. J.: IMERG V06: Changes to the Morphing
Algorithm, <https://doi.org/10.1175/JTECH-D-19-0114.1>, 2019b.

892

893 Tu, Q., Zhao, Y., Guo, J., Cheng, C., Shi, L., Yan, Y., and Hao, Z.: Spatial and Temporal Variations of
Aerosol Optical Thickness over the China Seas from Himawari-8, *Remote Sensing*, 13, 5082,
894 <https://doi.org/10.3390/rs13245082>, 2021.

895

896 Twomey, S.: Pollution and the planetary albedo, *Atmospheric Environment* (1967), 8, 1251–1256,
[https://doi.org/10.1016/0004-6981\(74\)90004-3](https://doi.org/10.1016/0004-6981(74)90004-3), 1974.

897

Twomey, S.: The Influence of Pollution on the Shortwave Albedo of Clouds, 1977.

898

899 Wall, C. J., Norris, J. R., Possner, A., McCoy, D. T., McCoy, I. L., and Lutsko, N. J.: Assessing effective
radiative forcing from aerosol–cloud interactions over the global ocean, *Proceedings of the National
Academy of Sciences*, 119, e2210481119, <https://doi.org/10.1073/pnas.2210481119>, 2022.

900

901 Wang, B., LinHo, Zhang, Y., and Lu, M.-M.: Definition of South China Sea Monsoon Onset and
902 Commencement of the East Asia Summer Monsoon, <https://doi.org/10.1175/2932.1>, 2004.

903

904 Wang, B., Huang, F., Wu, Z., Yang, J., Fu, X., and Kikuchi, K.: Multi-scale climate variability of the
South China Sea monsoon: A review, *Dynamics of Atmospheres and Oceans*, 47, 15–37,
905 <https://doi.org/10.1016/j.dynatmoce.2008.09.004>, 2009.

906

907 Wang, F., Guo, J., Wu, Y., Zhang, X., Deng, M., Li, X., Zhang, J., and Zhao, J.: Satellite observed
aerosol-induced variability in warm cloud properties under different meteorological conditions over



908 eastern China, *Atmospheric Environment*, 84, 122–132, <https://doi.org/10.1016/j.atmosenv.2013.11.018>,
909 2014.

910 Wang, J.-J., Li, X., and Carey, L. D.: Evolution, Structure, Cloud Microphysical, and Surface Rainfall
911 Processes of Monsoon Convection during the South China Sea Monsoon Experiment, *Journal of the*
912 *Atmospheric Sciences*, 64, 360–380, <https://doi.org/10.1175/JAS3852.1>, 2007.

913 Wang K.-Y., Sui C.-H., Lu M.-M., and Hong J.-S.: Cold Surge Impacts on the Structure, Energy Budget,
914 and Turbulence of the South China Sea Boundary Layer, <https://doi.org/10.1175/MWR-D-23-0238.1>,
915 2024a.

916 Wang, S., Wang, Q., and Feingold, G.: Turbulence, Condensation, and Liquid Water Transport in
917 Numerically Simulated Nonprecipitating Stratocumulus Clouds, 2003.

918 Wang, Y., Zhao, P., Xiao, H., and Zhang, P.: Aerosol effects on liquid cloud microphysical properties in
919 south China: Land–ocean contrasts, *Atmospheric Pollution Research*, 15, 102032,
920 <https://doi.org/10.1016/j.apr.2023.102032>, 2024b.

921 Wang, Y., Li, J., Fang, F., Zhang, P., He, J., Pöhlker, M. L., Henning, S., Tang, C., Jia, H., Wang, Y.,
922 Jian, B., Shi, J., and Huang, J.: In-situ observations reveal weak hygroscopicity in the Southern Tibetan
923 Plateau: implications for aerosol activation and indirect effects, *npj Clim Atmos Sci*, 7, 77,
924 <https://doi.org/10.1038/s41612-024-00629-x>, 2024c.

925 Wang, Y., Jia, H., Zhang, P., Fang, F., Li, J., Zhu, L., Wang, Y., Wang, T., and Li, J.: Sensitivity of cloud
926 microphysics to aerosols highly associated with cloud water content: Implications for indirect radiative
927 forcing, *Atmospheric Research*, 309, 107552, <https://doi.org/10.1016/j.atmosres.2024.107552>, 2024d.

928 Watters, D. and Battaglia, A.: The Summertime Diurnal Cycle of Precipitation Derived from IMERG,
929 *Remote Sensing*, 11, 1781, <https://doi.org/10.3390/rs11151781>, 2019.

930 Watters, D., Battaglia, A., and Allan, R. P.: The Diurnal Cycle of Precipitation according to Multiple
931 Decades of Global Satellite Observations, Three CMIP6 Models, and the ECMWF Reanalysis, *Journal*
932 *of Climate*, 34, 5063–5080, <https://doi.org/10.1175/JCLI-D-20-0966.1>, 2021.

933 Wu, Z., Jiang, C., Conde, M., Chen, J., and Deng, B.: The long-term spatiotemporal variability of sea
934 surface temperature in the northwest Pacific and China offshore, *Ocean Science*, 16, 83–97,
935 <https://doi.org/10.5194/os-16-83-2020>, 2020.

936 Xiao, H.-W., Xiao, H.-Y., Luo, L., Shen, C.-Y., Long, A.-M., Chen, L., Long, Z.-H., and Li, D.-N.:
937 Atmospheric aerosol compositions over the South China Sea: temporal variability and source
938 apportionment, *Atmospheric Chemistry and Physics*, 17, 3199–3214, <https://doi.org/10.5194/acp-17-3199-2017>, 2017.



940 Yost, C. R., Minnis, P., Sun-Mack, S., Chen, Y., and Smith, W. L.: CERES MODIS Cloud Product
941 Retrievals for Edition 4—Part II: Comparisons to CloudSat and CALIPSO, *IEEE Transactions on*
942 *Geoscience and Remote Sensing*, 59, 3695–3724, <https://doi.org/10.1109/TGRS.2020.3015155>, 2021.

943 Yuan, C.-S., Chuang, H.-L., Tseng, Y.-L., Li, T.-C., Soong, K.-Y., and Cheng, W.-H.: Long-range
944 transport and source apportionment of marine fine particles in the Taiwan Strait and South China Sea
945 Intersection: Spatiotemporal variations and chemical fingerprints, *Atmospheric Environment*, 339,
946 120867, <https://doi.org/10.1016/j.atmosenv.2024.120867>, 2024.

947 Yuan, T., Li, Z., Zhang, R., and Fan, J.: Increase of cloud droplet size with aerosol optical depth: An
948 observation and modeling study, *Journal of Geophysical Research: Atmospheres*, 113,
949 <https://doi.org/10.1029/2007JD008632>, 2008.

950 Zhang, C., Xu, H., Li, Z., Xie, Y., and Li, D.: Maritime Aerosol Optical and Microphysical Properties in
951 the South China Sea Under Multi-source Influence, *Sci Rep*, 9, 17796, <https://doi.org/10.1038/s41598-019-54483-6>, 2019.

953 Zhang, G. J., Ramanathan, V., and McPhaden, M. J.: Convection-Evaporation Feedback in the Equatorial
954 pacific, 1995.

955 Zhang, Y. and Wang, K.: The Changing Morphology of Global Precipitation Systems during the Last
956 Two Decades, *Bulletin of the American Meteorological Society*, 105, E1861–E1880,
957 <https://doi.org/10.1175/BAMS-D-23-0106.1>, 2024.

958 Zhao, C., Sun, Y., Yang, J., Li, J., Zhou, Y., Yang, Y., Fan, H., and Zhao, X.: Observational evidence
959 and mechanisms of aerosol effects on precipitation, *Science Bulletin*, 69, 1569–1580,
960 <https://doi.org/10.1016/j.scib.2024.03.014>, 2024.

961 Zheng, B., Qu, J., Huang, Y., Peng, D., Gu, D., Li, C., and Huang, R.: Evaluating the Seasonal Cycle of
962 the South China Sea Monsoon in CMIP6 Models, *J Meteorol Res*, 39, 322–337,
963 <https://doi.org/10.1007/s13351-025-4170-x>, 2025.

964 Zheng, H., Liu, M., Lohmann, R., Li, D., Vojta, S., Katz, S., Wang, W., Ke, H., Wang, C., and Cai, M.:
965 Gaseous polycyclic aromatic hydrocarbons over the South China Sea: Implications for atmospheric
966 transport under monsoon influences, *Marine Pollution Bulletin*, 191, 114982,
967 <https://doi.org/10.1016/j.marpolbul.2023.114982>, 2023.

968 Zheng, X., Xi, B., Dong, X., Wu, P., Logan, T., and Wang, Y.: Environmental effects on aerosol–cloud
969 interaction in non-precipitating marine boundary layer (MBL) clouds over the eastern North Atlantic,
970 *Atmos. Chem. Phys.*, 22, 335–354, <https://doi.org/10.5194/acp-22-335-2022>, 2022.

971 Zhu, S., Xiao, Z., Che, H., and Chen, Q.: Impact of aerosols on warm clouds over the Sichuan Basin,
972 China in winter based on the MERRA-2 reanalysis dataset, *Atmospheric Pollution Research*, 13, 101342,
973 <https://doi.org/10.1016/j.apr.2022.101342>, 2022.



974 Zhu, S., Li, Z., Chen, M., Wen, Y., Gao, S., Zhang, J., Wang, J., Nan, Y., Ferraro, S. C., Tsoodle, T. E.,
975 and Hong, Y.: How has the latest IMERG V07 improved the precipitation estimates and hydrologic
976 utility over CONUS against IMERG V06?, Journal of Hydrology, 645, 132257,
977 <https://doi.org/10.1016/j.jhydrol.2024.132257>, 2024.

978